Hindawi
Geofluids
Volume 2022, Article ID 1705985, 22 pages
https://doi.org/10.1155/2022/1705985

WILEY | Hindawi

Review Article

On the Freeze-Thaw Instability of an Open Pit Slope Using Three-Dimensional Laser Scanning and Numerical Simulation

Juzhou Li, Changhong Li, Guoqing Li, Yongyue Hu, Xuefeng Yi, and Yu Wang

Beijing Key Laboratory of Urban Underground Space Engineering, Department of Civil Engineering, School of Civil & Resource Engineering, University of Science & Technology Beijing, Beijing 100083, China

Correspondence should be addressed to Yu Wang; wyzhou@ustb.edu.cn

Received 13 May 2022; Accepted 11 July 2022; Published 31 July 2022

Academic Editor: Long Yan

In order to reveal the instability law of open pit mine slope in high-cold and high-altitude area. Firstly, the slope structural plane is scanned by three-dimensional (3D) laser scanning technology, and the point cloud data is obtained to realize the intelligent identification of rock mass structural plane. The geometric parameters of rock mass are counted, and the physical structure model is established. Then, we carry out freeze-thaw cyclic tests on granite to obtain the corresponding mechanical parameters. Finally, according to the obtained mechanical parameters, we use RS2 finite element software to calculate the shear strength of structural plane and joint by generalized Hoek-Brown criterion and Barton-Bandis criterion, respectively, establish the geomechanical model, and use the finite element strength reduction method to calculate the safety factor of slope and judge the instability of slope. The results show that the physical and mechanical properties of granite deteriorate with the increase of the freeze-thaw cycle. Under the action of the freeze-thaw cycle, the pore water in the rock mass freezes and forms frost heaving force. The expansion of volume leads to the further development of joint fissures. The strength of rock slope decreases gradually with the increase of freeze-thaw cycle times, and the safety factor of slope decreases continuously. It shows that repeated freeze and thaw alternation makes the stability of mine slope worse and worse. The research results are helpful to prevent the occurrence of slope disasters in advance and are of great significance to effectively and safely manage the stability of slope, the treatment of open pit, and environmental treatment.

1. Introduction

With the development of science and technology, 3D laser scanning technology and finite element software are widely used in the analysis of rock slope stability [1–3]. At the same time, in order to satisfy the growing production demand, China's mineral resources development has gradually shifted to the northwest region, which is rich in mineral resources but as poor natural environment, with weak infrastructure, poor ecological environment, and extremely cold winter. The temperature variation and seasonal variation caused by the alternation of day and night will have a great impact on the mechanical properties of rock mass. Repeated freeze-thaw cycle will expand and increase the rock fissures, deteriorate the physical and mechanical properties of the rock, and reduce the strength of the slope rock mass, resulting in the sliding of the slope rock mass [4–6]. These issues have become increasingly prominent. Therefore, this paper puts forward the research on the safety and stability evaluation of open pit slope based on 3D laser scanning and numerical simulation.

3D laser scanning is the latest development of geological mapping [7], which has been proved to be an effective noncontact tool. It is used to collect rock mass information. Its application fields include surface geological data collection [8, 9], slope stability and displacement monitoring [10, 11], and 3D rock mass model creation [12, 13]. It has the advantages of high density, maneuverability, high precision, and noncontact. At present, many experts and scholars have carried out a series of scanning analysis on rock slope engineering with the help of this technology. Chen et al. [14] compared the difference between 3D laser scanning technology and traditional window mapping technology. The results show that the average dip/dip direction discrepancy between the two methods is 1.5°/16°, which is due to the large amount of data collected by 3D laser scanning technology. It is proved that the 3D laser scanning technology has the advantages of higher efficiency and accuracy in underground mines. Wang et al. [15] used 3D laser scanning technology to scan the fragmentation of blast muck piles and provided high-precision point cloud data for calculating BFMP. They proposed an improved VCCS algorithm based on discrete characteristics. The results show that when the size of crushing block is 0.1 m ~0.5 m, the accuracy of calculation results are about 80%, and when the size of broken block exceeds 0.5 m, almost all bfmp can be calculated correctly. Kromer et al. [16] used a ground-based 3D laser scanning technology to test the Séchiienne landslide in France for six weeks to detect the flow, displacement, and prefailure deformation of discrete collapse events. Then, they proposed an automatic ground laser scanning system with near real-time automatic change detection and processing function. Ma et al. [17] introduced 3D laser scanning technology into the overall deformation monitoring of slope surface in landslide physical model test and comprehensively analyzed the deformation characteristics of landslide in different evolution stages through the example of landslide physical model test. The results show that on the premise of ensuring high-precision feature point monitoring, the overall deformation and displacement of the model slope can be obtained with the help of 3D laser scanning technology.

Similarly, RS2 software can carry out fluid structure coupling analysis and dynamic analysis and can automatically generate finite element meshes such as triangles, and material models have the advantages of diversified types. It is also widely used in numerical simulation under cyclic loading [18]. In order to analyze the yield failure of the open pit mine in Minas Gerais, Brazil, Pereira and Lana [19] established many representative slope hypothesis models by using RS2 finite element software, carried out elastic and plastic simulation, and evaluated the yield failure mechanism. Liu et al. [20] used numerical simulation software to study the main causes of coal mine roof accidents. The results show that as the coal seam continues to advance, the maximum settlement displacement remains basically unchanged, and the settlement displacement curve presents an asymmetric flat bottom distribution and the stress concentration in front of the coal wall is the source of the abutment pressure. Silva and Lana [21] used RS2 software to study the failure mechanism of flexural buckling that occurred in Pau Branco Mine, of Vallourec and Mannesman Group, in 2002. Through the back analysis of the failure mechanism, they obtained the representative values of in situ stress state, normal stiffness modulus, and shear stiffness modulus of foliation structure. The results are of great significance to further analyze the stability of phyllite slopes of Pau Branco Mine. Arslan et al. [22] used RS2 finite element software to analyze the stability of marble stope under static and dynamic conditions, built shear strength reduction (SSR) technology into the software to determine the failure mechanism, and put forward suggestions and carried out necessary control to ensure the stability of slope. Adach-Pawelus [23] used RS2 finite element software to conduct numerical simulation in the plane deformation state, combined with seismic activity analysis and numerical simulation methods to illustrate the impact of mine residues on the possibility of seismic events. The results show that undisturbed rock cuttings may have a negative impact on earthquake and rock burst disasters in the mining area.

Even though 3D laser scanning technology and RS2 finite element software have made great progress and application, there are few studies on high-cold and high-altitude areas with the help of and combination of these two technologies. In view of this, this paper uses Optech Polaris LR 3D laser scanner to scan the open pit slope in cold area, obtains the point cloud data, realizes the intelligent identification and information extraction of rock mass structural plane, obtains the rock mechanical parameters through the freeze-thaw cycle tests, and establishes the slope mechanical model combined with RS2 finite element software to calculate the safety factor of the slope under different times of freeze-thaw cycle. This has important guiding significance for in-depth understanding of the law of slope instability of open pit mines in high-cold and high-altitude areas and preventing slope disasters and accidents in advance [24].

2. Identification and Extraction of Rock Structure Plane

2.1. Study Area. The research object of this paper is located in Beizhan iron mine in Hejing County, Korla, Xinjiang, in Northwest China. Permanent Piedmont glaciers are located in the south and west of the mining area, and the altitude of the ore body is 3450-3723 m. The mining area is located in the alpine area with perennial snow, and the climate is extremely cold. The monthly average temperature from January to April and from September to December is lower than zero, and the minimum temperature can reach -40°C. The temperature rises from May to August, generally 5-15°C, and the maximum rise can be 20°C. The temperature at night is usually as low as about -3°C, so the temperature difference between day and night in the mining area is large. The mining area has frequent rain and snow throughout the year. It is the local rainy season from July to August, and it begins to snow in early October. Therefore, it is only suitable to carry out appropriate field operations from May to September every year. The deposit is located in the river valley, and the terrain of the mining area is conducive to natural drainage. The overall strike of the ore body is 97°, and the dip angle is 47°-74°. According to the prediction of landform, meteorology and hydrology, geological structure, human activities, and other conditions in the mining area, the risk of geological disasters such as landslide and debris flow is small, but the risk of collapse geological disasters caused by local high and steep mountains is high. The study area is shown in Figure 1.

2.2. 3D Laser Scanning Technique. Optech Polaris LR 3D laser scanner is used to conduct overall scanning and fine scanning of the research area, respectively. The instrument

Figure 1: Study area.

Figure 2: Placement of 3D laser scanner.

Table 1: Parameters of 3D laser scanner.

Parameters	Index
Maximum measuring distance (m)	2000
Minimum measuring distance (m)	1.5
Scanning vision angle (°)	360 × 120
Principle of distance measuring	Pulse
Laser head rotation mechanism	Swinging mirrors
Working temperature (°C)	-20~50

meets the long-distance fine test requirements of the project, as shown in Figure 2. The parameters are shown in Table 1.

2.3. Rock Structural Plane Geometric Characteristics. In order to have a preliminary understanding of the whole mining area, 11 3D laser scans were carried out, covering the whole mining pit, as shown in Figure 3(a). 3D laser scanning was carried out on each point to obtain the point cloud data of each point. After splicing and packaging, a complete 3D geometric model is obtained, as shown in Figure 3(b). At the same time, fine scanning is carried out for the mining area. The scanning point S8 is located on the east side of the pit, including 399020 points. The scanning range is 2044.0957 m^2, and the maximum size of the scanning area is $51.2365 \times 61.8522 \times 29.0181$ m. Combining the 3D laser scanning technology with the digital camera, the pixel points of the picture are matched with the point cloud, and the gray information or color information of the point cloud data can be obtained. The color information is helpful to display the scanning results, and the results are shown in Figure 3(c).

2.3.1. Processing of Point Cloud Data. The amount of point cloud data obtained by 3D laser scanning structural plane is large and dense will seriously affect the operation speed. Therefore, in order to realize the programming of the algorithm, it is necessary to divide the point cloud data into space and grid the point cloud data. In this study, for the point cloud data with high scanning accuracy, the 3D difference method is adopted. This method has little impact on the accuracy, and the impact can be ignored. The results are shown in Figure 4.

In order to obtain the optimal threshold, it is necessary to select the discrimination index of structural plane intelligent recognition. In this paper, the point normal vector is used as the discrimination index. The next step is to determine the flatness detection threshold of point cloud.

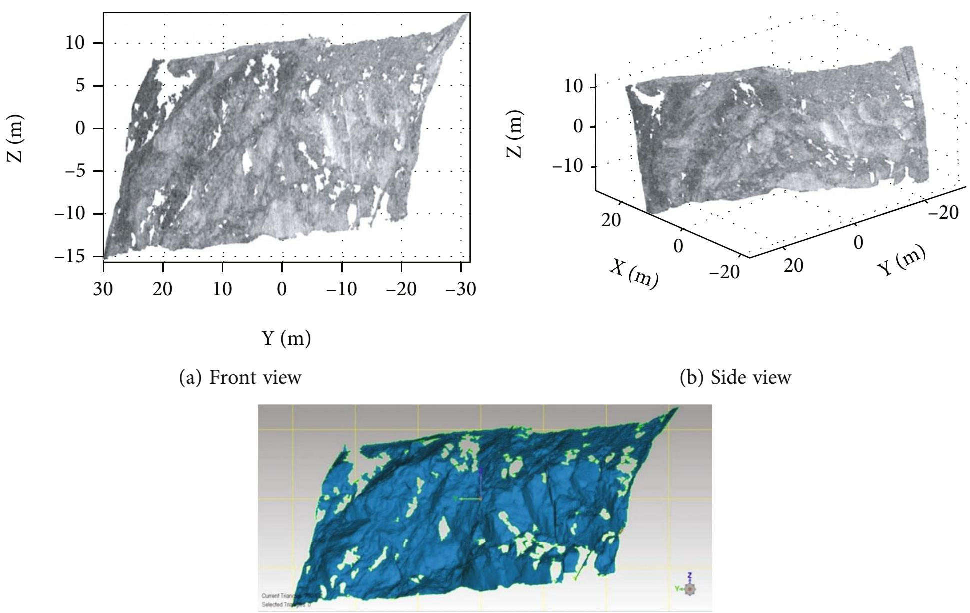

(a) Front view

(b) Side view

(c) Triangulation model

Figure 3: S8 station scanning slope point cloud data.

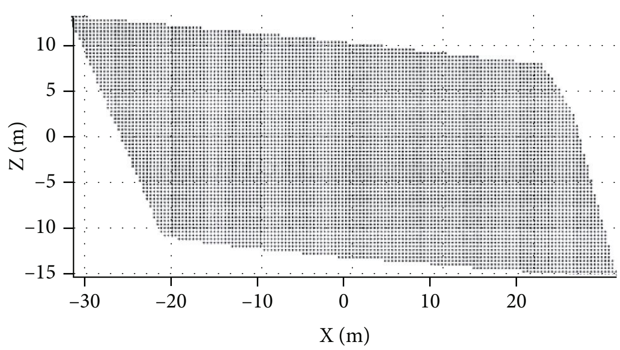

Figure 4: Result of grid processing.

According to the rules, when the value of ξ_1 is smaller, the more points are included in the BORDER matrix, which means that more points are regarded as boundary points and do not participate in the next image segmentation algorithm. Conversely, when the value of ξ_1 is too large, the number of points in the BORDER matrix decreases, which means that the edge recognition effect is weakened, indicating that some boundary points will not be recognized effectively. So, according to the actual situation of the mining area, the flatness detection threshold ξ_1 is set to 20°.

2.3.2. Selection of Optimal Threshold. Make the regional growth threshold ξ_2 between 5° and approximately 40°, and the value interval is 5°. The area threshold remains unchanged at 0.5 m^2. When the value of regional growth threshold is too small, the growth criteria is relatively severe, and many point cloud data are not identified as structural plane, which makes the regional division too fragmented and the number of structural plane identified is few. When the value of regional growth threshold is too large, the growth criteria is too loose, which leads to a part of the point cloud data located in uneven areas will also be divided into structural plane, and the number of structural plane identified is too large, so it is impossible to distinguish adjacent structural plane. According to visual judgment, when the regional growth threshold is between 20° and 30°, the recognition effect is more realistic. The results of structural plane recognitions are shown in Figures 5(a)–5(c).

Similarly, make the area threshold W_1 between 0.1 m^2 and approximately 10 m^2, and the value interval is 0.1 m^2. The regional growth threshold remains unchanged at 20°. When the area threshold W_1 is greater than 0.1 m^2, the recognition effect is more practical. When the area threshold is too large, more structural plane are eliminated, which leads to too few remaining structural plane and is not conducive to the later structural plane information extraction. The result of structural plane recognition is shown in Figure 5(d). In summary, the growth threshold is 20°, and the area threshold is 0.1 m^2.

2.4. Extraction of Structural Plane Information of Rock Mass

2.4.1. Acquisition of Structure Plane Occurrence Information. The least square method is used to fit all nodes of each rock mass structural plane obtained before. In this way, the plane equation of quasi plane shape can be obtained. The plane equation is shown in

$$ax + by + c = z. \tag{1}$$

It is assumed that the spatial coordinates of n points on the structural plane are (x_1, y_1, z_1), (x_2, y_2, z_2) ,…,(x_n, y_n, z_n), respectively, and the matrix equation can be expressed as

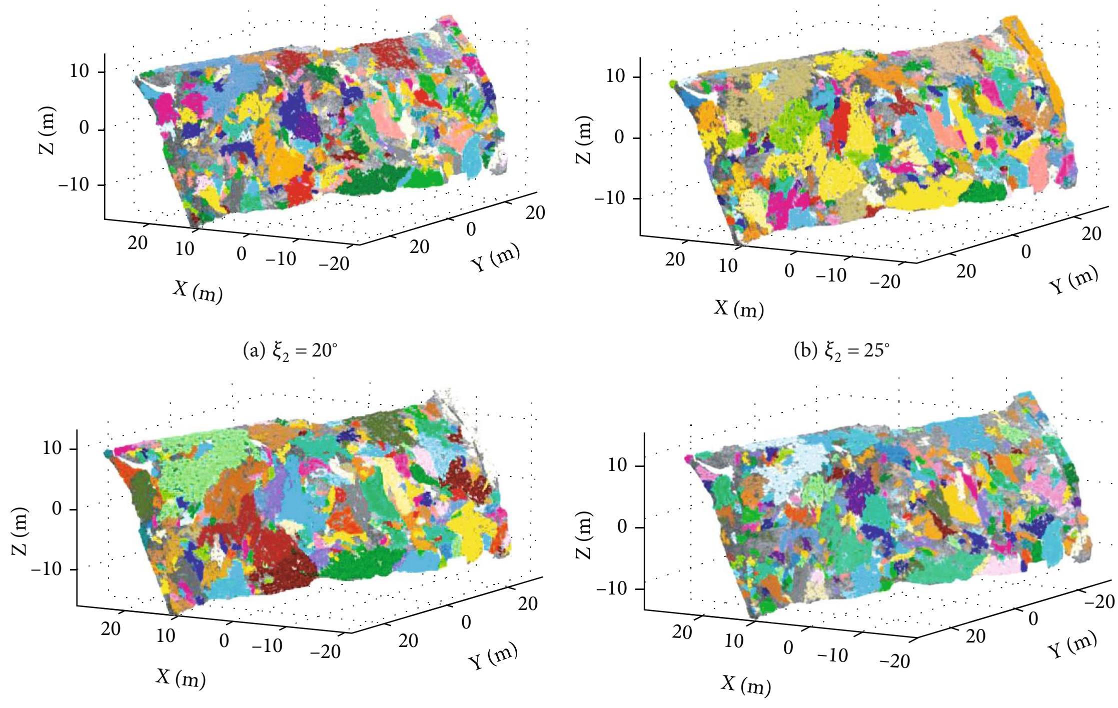

(a) $\xi_2 = 20^{\circ}$

(b) $\xi_2 = 25^{\circ}$

(c) $\xi_2 = 30^{\circ}$

(d) $W_1 = 0.1\,\text{m}^2$

Figure 5: Intelligent identification results of rock structural plane under different growth and area thresholds.

$$\begin{bmatrix} x_1 & y_1 & 1 \\ x_2 & y_2 & 1 \\ \vdots & \vdots & \vdots \\ x_n & y_n & 1 \end{bmatrix} \begin{bmatrix} a \\ b \\ c \end{bmatrix} = \begin{bmatrix} z_1 \\ z_2 \\ \vdots \\ z_n \end{bmatrix}. \tag{2}$$

Let

$$D = \begin{bmatrix} a \\ b \\ c \end{bmatrix}, \tag{3}$$

$$X = \begin{bmatrix} x_1 & y_1 & 1 \\ x_2 & y_2 & 1 \\ \vdots & \vdots & \vdots \\ x_n & y_n & 1 \end{bmatrix}, \tag{4}$$

$$Z = \begin{bmatrix} z_1 \\ z_2 \\ \vdots \\ z_n \end{bmatrix}. \tag{5}$$

So, we need to find vector D and make $\phi(D) = \|DX - Z\|$ get the minimum value. Finally, the normal vector and plane equation of structural plane are obtained to complete the fitting of the structural plane.

This study mainly calculates the dip and dip angle in the occurrence information of structural plane. If the normal vector coordinate of structural plane is (x_0, y_0, z_0). According to the working principle of laser emission in 3D laser scanning technology, it can only scan the structural plane with good exposure on the side slope, so $z_0 > 0$. With the geodetic coordinate system, the due east and due north are defined as the positive directions of the X axis and Y axis, respectively, and the Z axis points to the elevation direction. Therefore, the occurrence information dip θ and dip angle δ of the rock mass structural plane can be expressed by the following equation:

$$\left.\begin{array}{l} \delta = \arccos(z_0) \\ \text{if} \quad x_0 \geqslant 0, y_0 \geqslant 0,\ \theta = \arcsin\left(\dfrac{x_0}{\sin\delta}\right) \\ \text{if} \quad x_0 < 0, y_0 > 0,\ \theta = 360^{\circ} - \arcsin\left(-\dfrac{x_0}{\sin\delta}\right) \\ \text{if} \quad x_0 < 0, y_0 > 0,\ \theta = 180^{\circ} - \arcsin\left(\dfrac{x_0}{\sin\delta}\right) \\ \text{if} \quad x_0 > 0, y_0 < 0,\ \theta = 180^{\circ} + \arcsin\left(-\dfrac{x_0}{\sin\delta}\right) \end{array}\right\}. \tag{6}$$

The occurrence information of point cloud data of rock mass structural plane is shown in Figure 6.

2.4.2. Grouping of Rock Mass Structure Planes Based on Occurrence Information. Then, the K-means cluster analysis method is used to group these occurrence information and is combined with the field investigation of geological

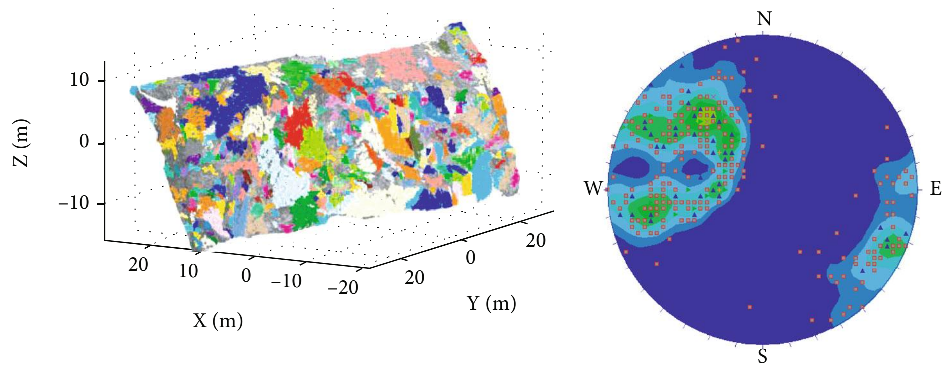

(a) Distribution characteristics of structural plane (b) The result of stereographic projection

Figure 6: Distribution characteristics of structural plane and the result of stereographic projection.

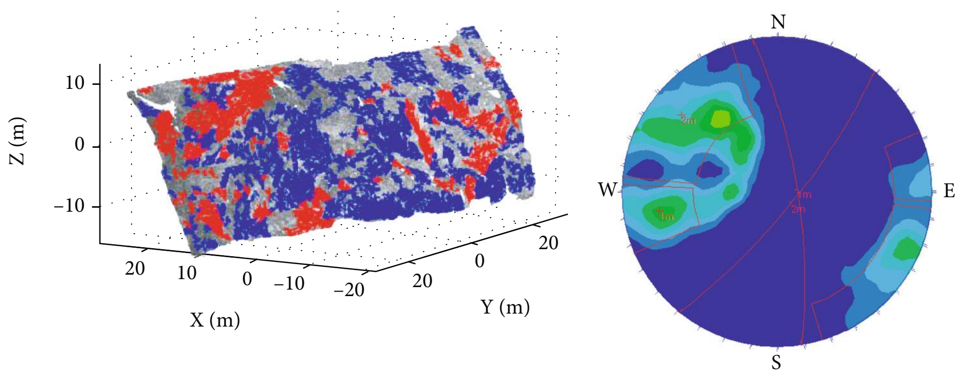

(a) Distribution characteristics of occurrence (b) The result of stereographic projection

Figure 7: Occurrence distribution characteristics of the rock mass structural plane after clustering and the result of stereographic projection.

information. It is obtained that the structural plane of the slope in the mining area can be divided into three groups, including a group of gently inclined plane and two groups of steeply inclined joints. Intelligent identification mainly finds two groups of steep joints. Finally, the cluster center and average occurrence are calculated. The average occurrence of the two groups of rock mass structural planes is $261° < 75°$ and $307° < 77°$, respectively. The results are shown in Figure 7.

In this study, the structural plane occurrence modeling method based on empirical probability distribution is adopted to truly reflect the actual structural plane occurrence distribution and then obtain the relative frequency of two groups of rock mass structural plane occurrence. The results are shown in Figure 8.

2.4.3. Calculation of Spacing between Rock Structural Planes. In order to obtain the spacing between adjacent structural planes, it is calculated according to the method shown in Figure 9. The dotted line in the figure is the initial state of the same group of structural planes, the solid line is the ideal state of the structural planes converted according to the above method, and the structural planes are parallel to each other in the same group. The vertical distance calculation equation is used to calculate the distance between adjacent structural planes.

$$l_1 : Ax + By + Cz + D_1 = 0, \tag{7}$$

$$l_2 : Ax + By + Cz + D_2 = 0, \tag{8}$$

$$d_{l_1 l_2} = \frac{|D_1 - D_2|}{\sqrt{A^2 + B^2 + C^2}}, \tag{9}$$

Where l_1 is plane 1 equation, l_2 is plane 2 equation, and $d_{l_1 l_2}$ is the vertical distance between two adjacent structural planes.

According to the equation, the distribution characteristics of the spacing information of the two groups of rock mass structural planes are calculated, as shown in Figure 10.

2.4.4. Calculation of Equivalent Trace Length of Rock Mass Structural Planes. Because the data obtained by the image segmentation method is point cloud data, the method of projection is used to calculate the area of the structural plane, as shown in

$$S = \frac{S_{xoy}}{\cos \gamma}, \tag{10}$$

where γ is the angle between the xoy plane and the structural plane, S is the area of the desired structural plane, and

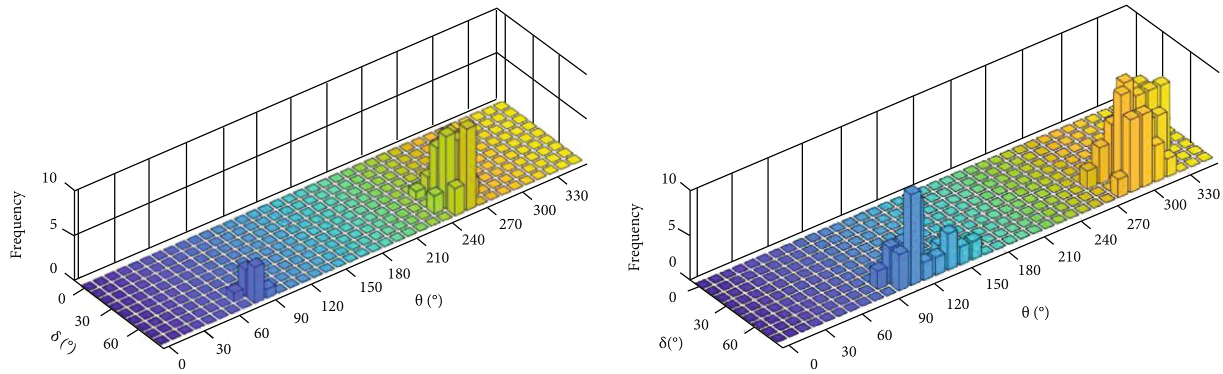

Figure 8: 3D histogram of the occurrence relative frequency of the structural plane of the two groups of rocks.

S_{xoy} is the projected area of the node on the structural plane projected onto the *xoy* plane.

Thus, the exposed area of rock mass structural plane is calculated. For convenience, the structural plane can be replaced by an equivalent circle with equal area. The radius is expressed in

$$S = \pi r^2. \tag{11}$$

The equivalent trace length of the two groups of rock mass structural planes in this paper can be characterized by the equivalent radius obtained by equation (11). The results are shown in Figure 11.

2.4.5. Statistics of Structural Plane Information of Rock Mass. Based on the theory of mathematical statistics, according to the point cloud data of S8 rock slope, the probability distribution types and statistical parameters of geometric parameters such as the occurrence of rock mass structural plane calculated above are counted, as shown in Table 2.

3. Numerical Simulation Analysis

In this paper, RS2 elastic-plastic finite element software is used for numerical simulation analysis. An important function of RS2 is to calculate the safety factor of slope stability based on the finite element strength reduction method. By using the Hoek-Brown strength criterion, the system can automatically reduce the strength and obtain the safety factor of the slope. In this software, the constitutive model of rock mass includes the generalized Hoek-Brown model, Mohr-Coulomb model, and Cam-Clay model. At the same time, based on the statistical model, users can input relevant joint parameters according to the actual situation when building the slope model, and the system will automatically generate the joint fracture network.

3.1. Establishment of Model and Selection of Parameters. In order to obtain the relevant mechanical parameters of rock slope and establish a complete geomechanical model, samples were taken from the site and divided into 6 groups with 2 samples in each group. The samples of each group were subjected to 0, 20, 40, 60, 80, and 100 times of freeze-thaw cycle, respectively, and physical and mechanical tests were

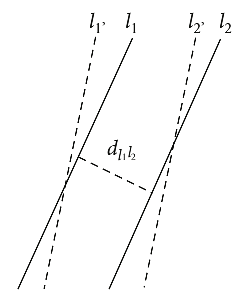

Figure 9: Plots of the 7same group of structural surface space distance by calculating.

carried out. Finally, the parameters shown in Table 3 are counted.

We intercepted a section line on the west slope of the mining area to automatically generate the section map of the west slope, import it into RS2 software, and generate the model boundary. The structural plane of rock mass is based on the generalized Hoek-Brown criterion, and the joint is a constitutive model based on Barton-Bandis criterion. According to the previous research, the slope is mainly affected by two sets of joint surfaces. The above physical and mechanical parameters were input into RS2 software, and the three node triangular element was used to generate the finite element grid. The model contained 17207 nodes and 29427 elements. We considered the actual boundary conditions on site and get the final result, as shown in Figure 12. Finally, five monitoring points were arranged for subsequent research.

3.2. Numerical Simulation Results

3.2.1. Analysis of Maximum Principal Stress and Maximum Shear Strain of Slope Model. According to the definition of principal stress, under the same external force, the principal stress increases with the increase of buried depth. In order to study the variation of the maximum principal stress under different times of freeze-thaw cycle, the cloud chart of the maximum principal stress is obtained as shown in Figure 13. It can be found from the figure that the maximum principal stress at the bottom of the slope model is greater than that in other areas, while the top is the smallest. At the same time, the value range of the maximum principal

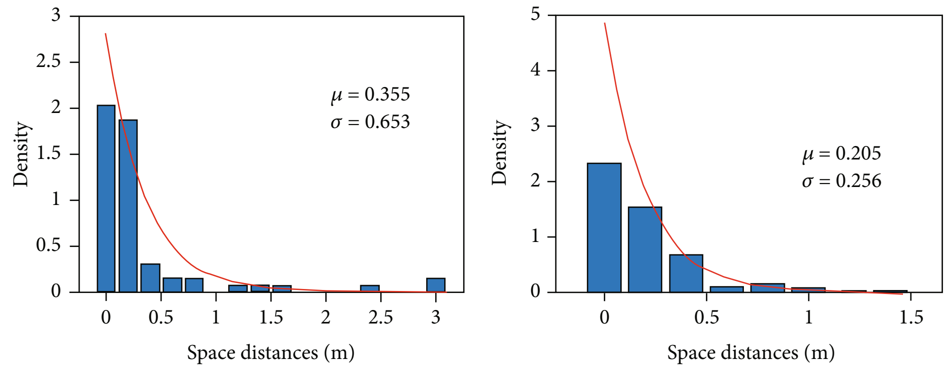

FIGURE 10: Histogram of space distance distribution of two groups of the rock mass structure plane.

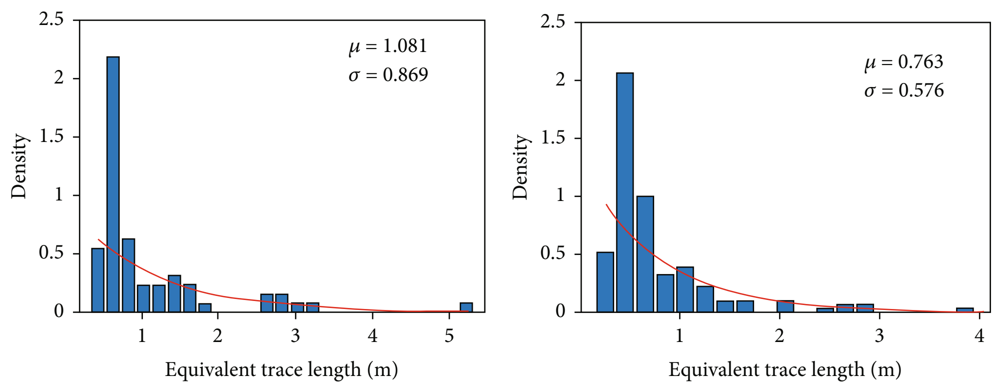

FIGURE 11: Histogram of equivalent trace length distribution of two groups of rock mass structure plane.

TABLE 2: Mathematical statistical information of rock mass structural planes.

Parameters	Distribution Type	Statistical parameters	Structure plane	Value
Tendency (°)	Empirical probability	Mean	Plane 1	261.000
			Plane 2	309.000
		Standard deviation	Plane 1	61.942
			Plane 2	103.558
Dip angle (°)	Empirical probability	Mean	Plane 1	75.000
			Plane 2	77.000
		Standard deviation	Plane 1	9.266
			Plane 2	10.173
Space distances (m)	Negative exponential distribution	Mean	Plane 1	0.355
			Plane 2	0.205
		Standard deviation	Plane 1	0.653
			Plane 2	0.256
Equivalent trace length (m)	Negative exponential distribution	Mean	Plane 1	1.081
			Plane 2	0.763
		Standard deviation	Plane 1	0.869
			Plane 2	0.576

stress does not change with the increase of the times of the freeze-thaw cycle and generally shows a slight upward trend, but it is between -0.75 MPa and 14.25 MPa. This shows that the increase of times of freeze-thaw cycle has little effect on the maximum principal stress of the slope.

In order to reflect the influence of different times of the freeze-thaw cycle on slope failure and instability, the cloud chart of corresponding maximum shear strain is obtained by numerical simulation, as shown in Figure 14. It can be seen from the figure that the safety factor decreases with

Table 3: Basic mechanical and physical parameters of freeze-thaw-treated granite samples.

Sample number	Length × width (mm × mm)	Mass (kg)	Density (g/cm^3)	Peak strength (MPa)	Elasticity modulus (MPa)	P-wave velocity (m/s)	S-wave velocity (m/s)
y0-1	100.07 × 49.46	541.4	2.863	172.38	58.65	4302	3577
y0-2	100.01 × 49.62	540.5	2.796	182.45	60.08	4412	3456
y20-1	99.58 × 49.30	543.1	2.859	168.73	56.31	4131	3391
y20-2	100.01 × 50.21	540.2	2.729	167.24	55.46	4265	3325
y40-1	99.85 × 50.05	542.6	2.763	163.98	52.78	4012	3101
y40-2	100.12 × 49.63	544.9	2.815	158.35	53.44	4000	3210
y60-1	100.22 × 49.85	547.5	2.800	158.78	50.89	3906	2984
y60-2	100.06 × 49.19	544.6	2.865	155.66	49.65	3894	3015
y80-1	99.90 × 49.88	548.9	2.813	152.39	47.36	3826	2883
y80-2	100.11 × 49.76	543.5	2.793	149.23	45.23	3856	2913
y100-1	100.12 × 49.29	547.2	2.866	146.65	42.94	3690	2664
y100-2	100.08 × 49.34	546.6	2.858	142.33	43.89	3546	2703

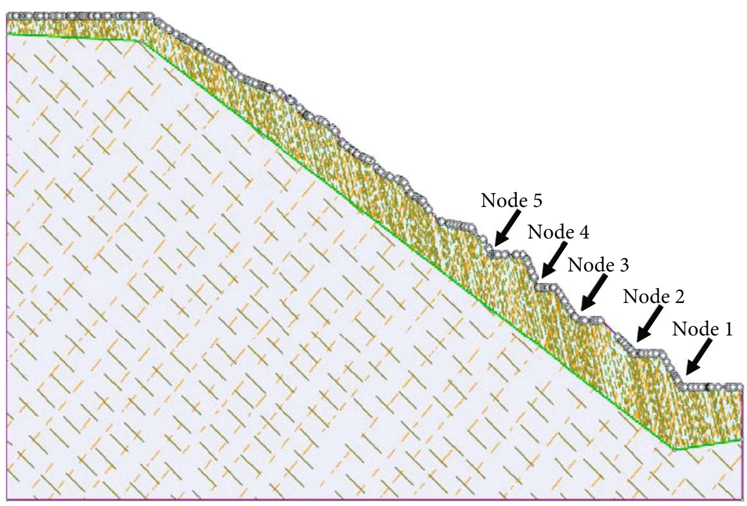

Figure 12: Contour map of Beizhan iron mine and slope calculation model.

the increasing times of the freeze-thaw cycle. At the same time, the maximum shear strain reflects the relative deformation of slope failure. The figure also shows that the relative deformation of failure gradually increases with the increase of the times of the freeze-thaw cycle. Because this paper studies the rock slope, it will not form a complete sliding zone like the soil slope. However, local rock mass spalling and instability failure will occur within the freeze-thaw shear area of the slope. The results show that the times of the freeze-thaw cycle has a great impact on the strength and stability of slope rock mass. The more times of the freeze-thaw cycle, the more serious the deterioration of internal performance of rock mass and the lower the stability of slope.

3.2.2. Analysis of Total Displacement of Slope Model. Figure 15 shows the change of total displacement nephogram of slope rock mass under different times of the freeze-thaw cycle. It can also be found from the figure that the safety factor decreases gradually with the increase of the times of the freeze-thaw cycle. At the same time, due to the self-weight of the overlying rock mass and mechanical excavation, the total displacement reaches the maximum in the first two steps.

According to the numerical simulation results, the strength reduction factor decreases with the increasing times of the freeze-thaw cycle. In order to further reflect the relationship between the strength reduction factor and the total displacement of the slope, the curve shown in Figure 16 is drawn. It can be clearly seen from the figure that under the same times of the freeze-thaw cycle, the initial increase of the maximum total displacement of the slope is not obvious, and then with the continuous increase of the strength reduction factor, the maximum total displacement changes abruptly and increases significantly. This shows that the slope is obviously damaged when the strength reduction

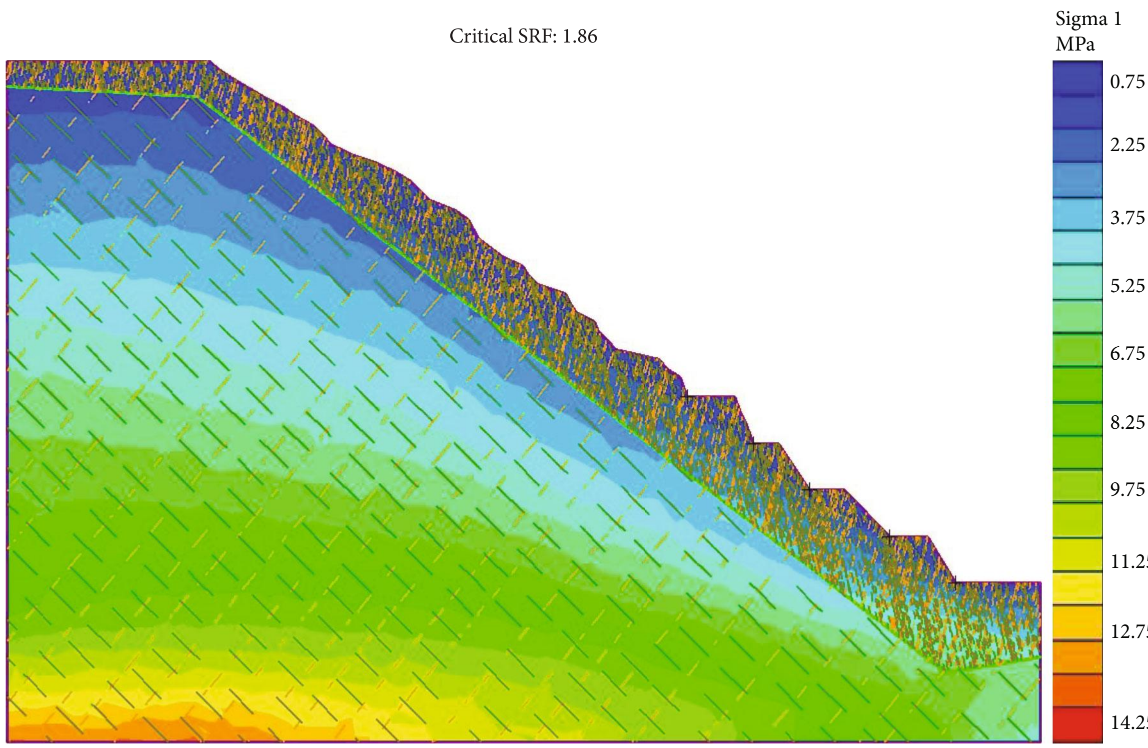

(a) Cloud chart of maximum principal stress for 0 times of the freeze-thaw cycle

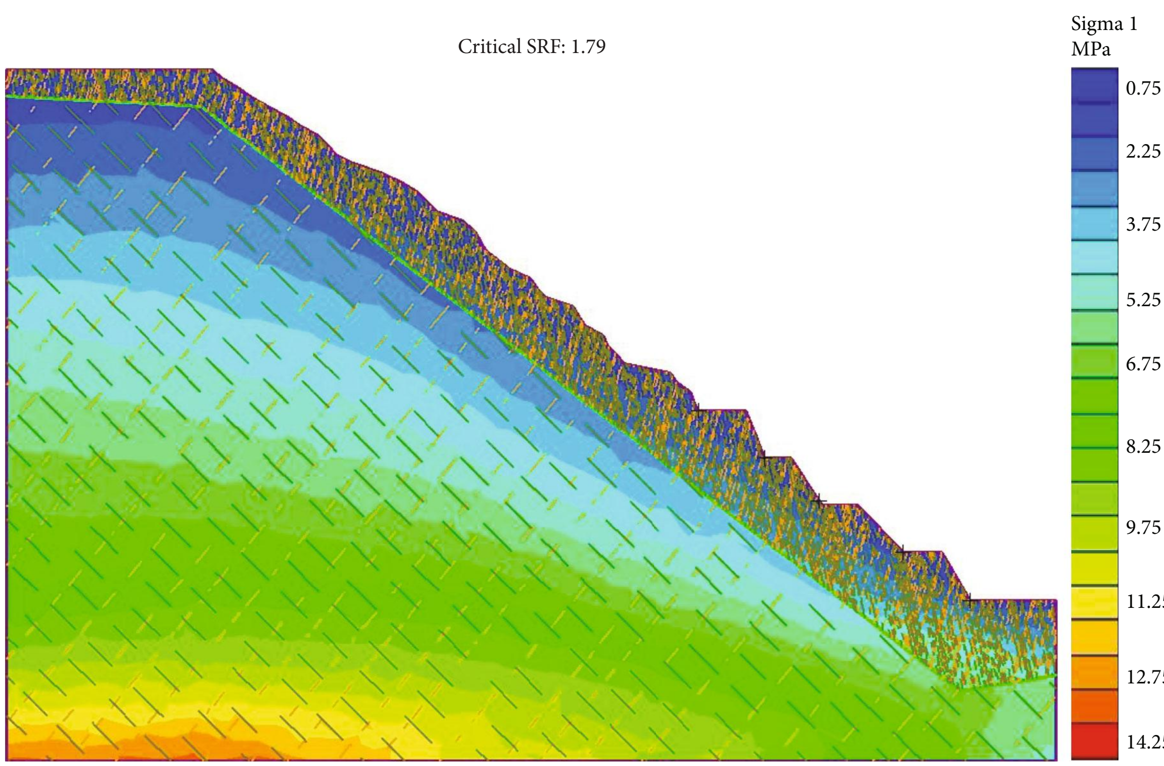

(b) Cloud chart of minimum principal stress for 20 times of the freeze-thaw cycle

Figure 13: Continued.

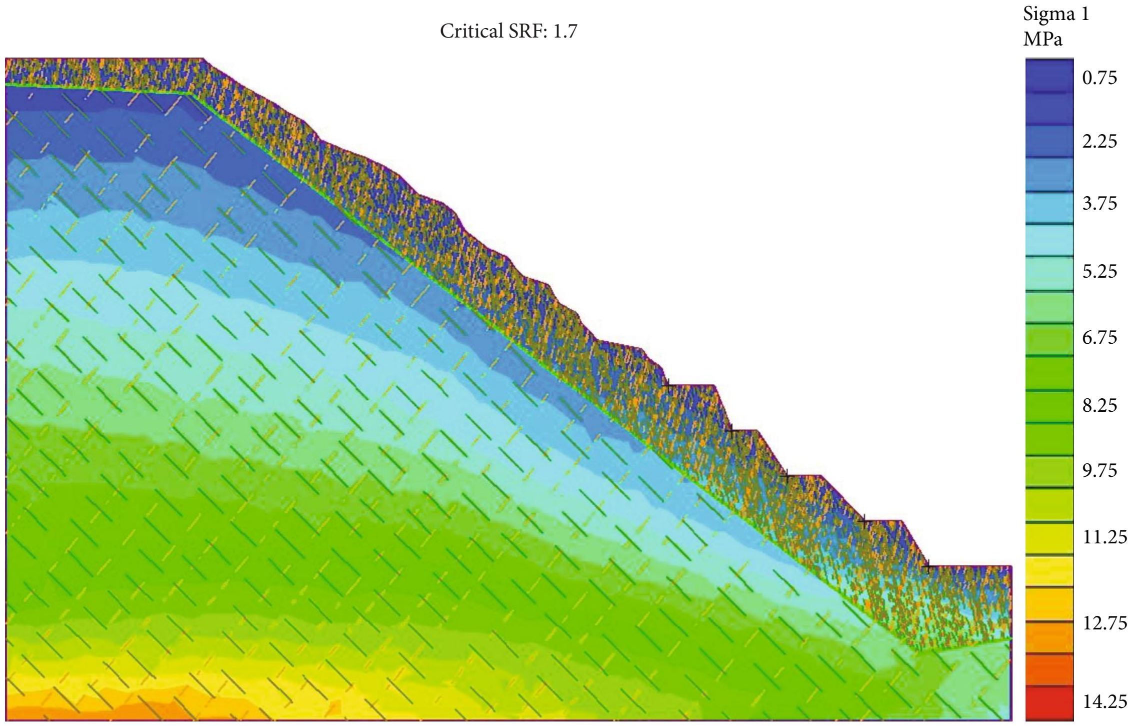

(c) Cloud chart of maximum principal stress for 40 times of the freeze-thaw cycle

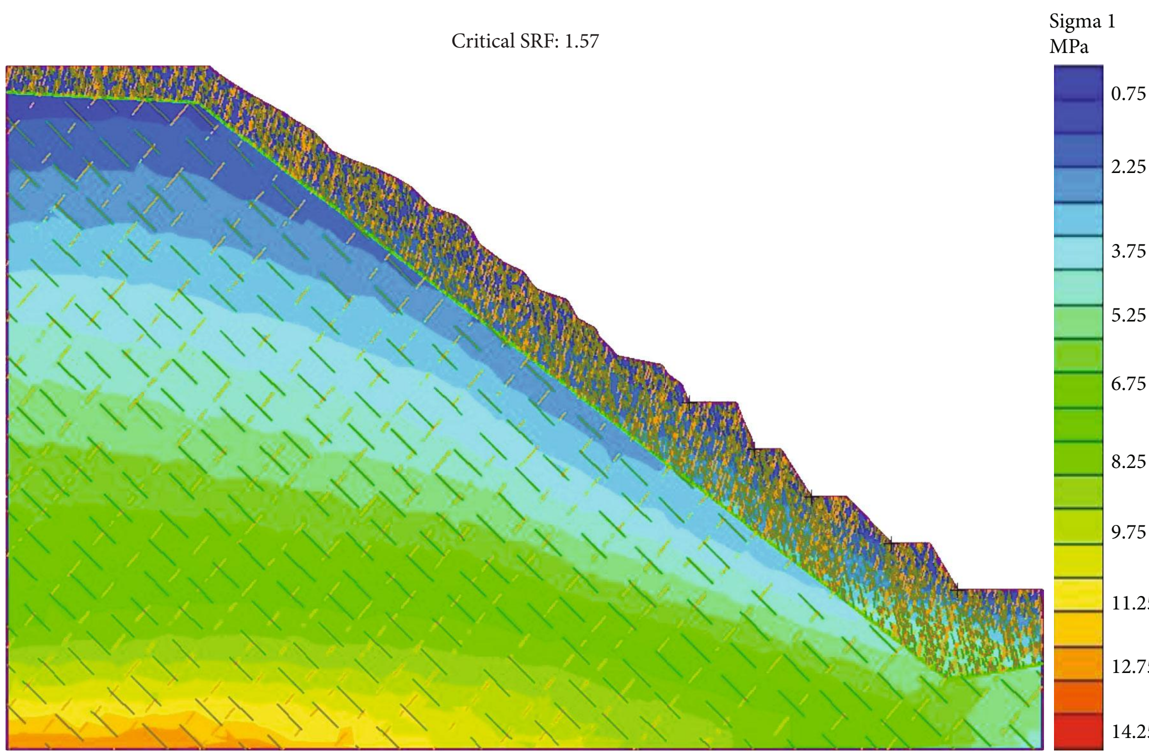

(d) Cloud chart of maximum principal stress for 60 times of the freeze-thaw cycle

FIGURE 13: Continued.

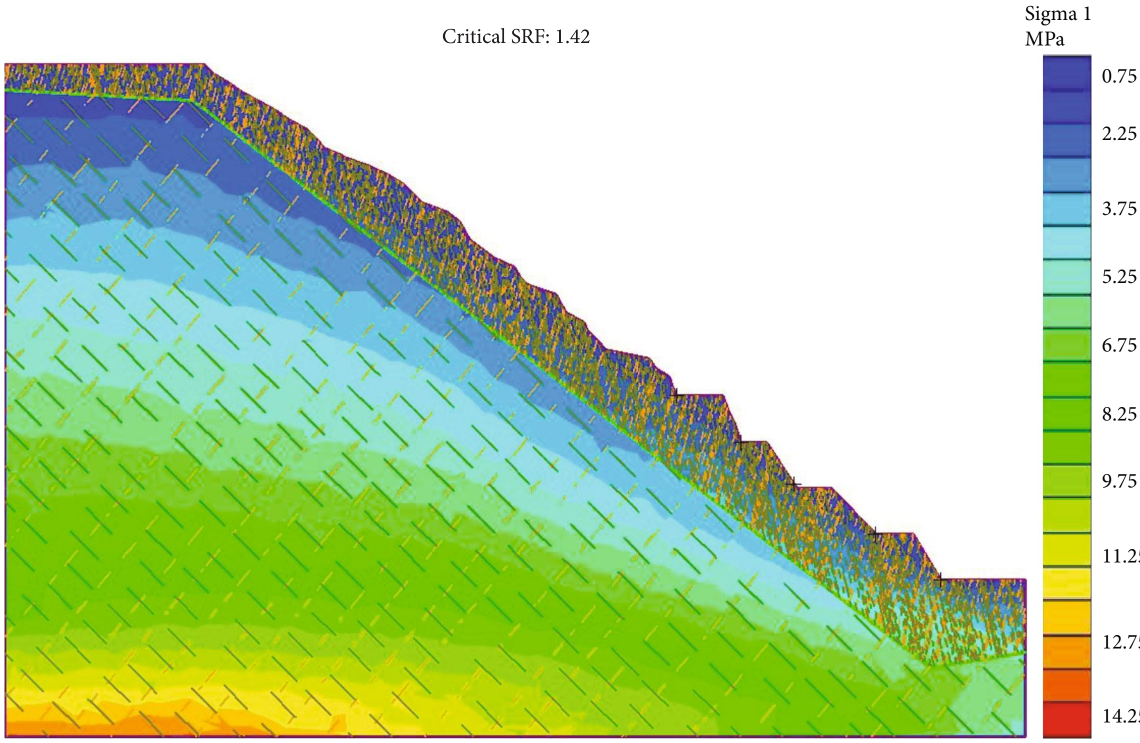

(e) Cloud chart of maximum principal stress for 80 times of the freeze-thaw cycle

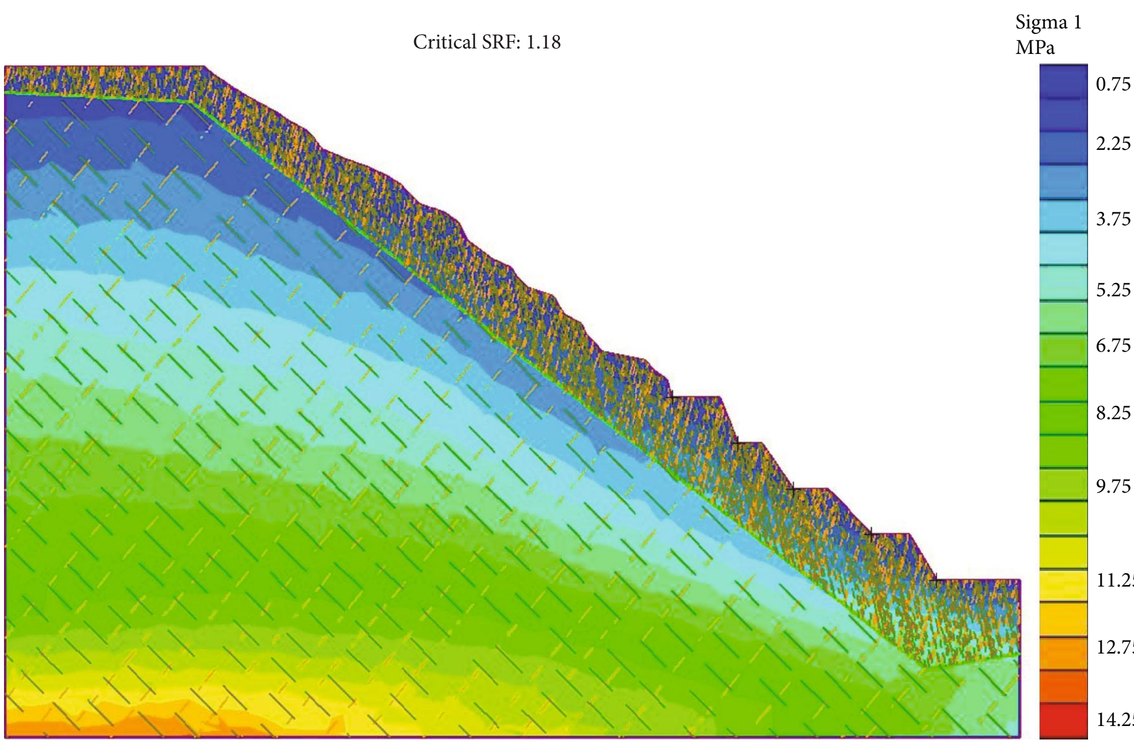

(f) Cloud chart of maximum principal stress for 100 times of the freeze-thaw cycle

FIGURE 13: Cloud chart of maximum and minimum principal stress for different times of the freeze-thaw cycle.

factor reaches this value. When the times of the freeze-thaw cycle increases, the strength reduction factor decreases gradually, and the decreasing range is larger and larger. It shows that the freeze-thaw cycle has a great weakening effect on the mechanical properties of slope rock mass.

3.2.3. Analysis of Yield Elements and Yield Joints of Slope Model. The number of yield elements, yield joints, and their distribution can well show the specific failure degree and failure area of rock. According to the previous test results, the physical and mechanical properties of slope rock mass deteriorate due

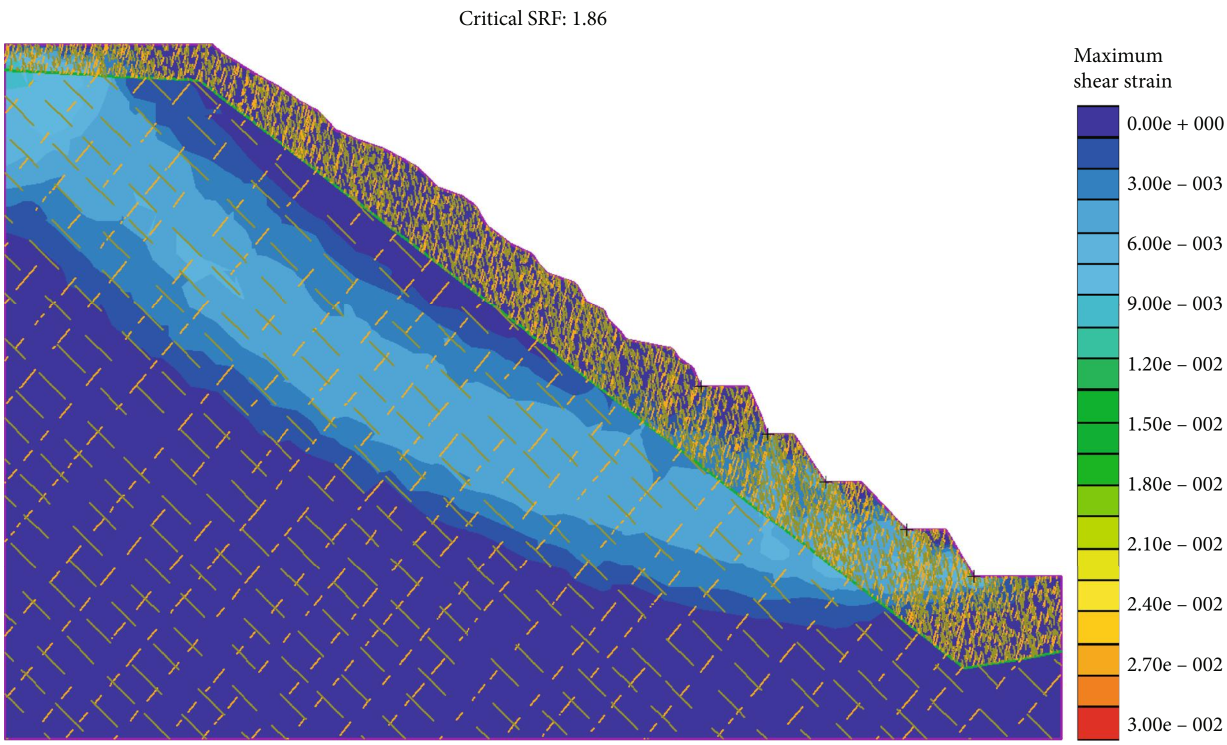

(a) Cloud chart of maximum shear strain for 0 times of the freeze-thaw cycle

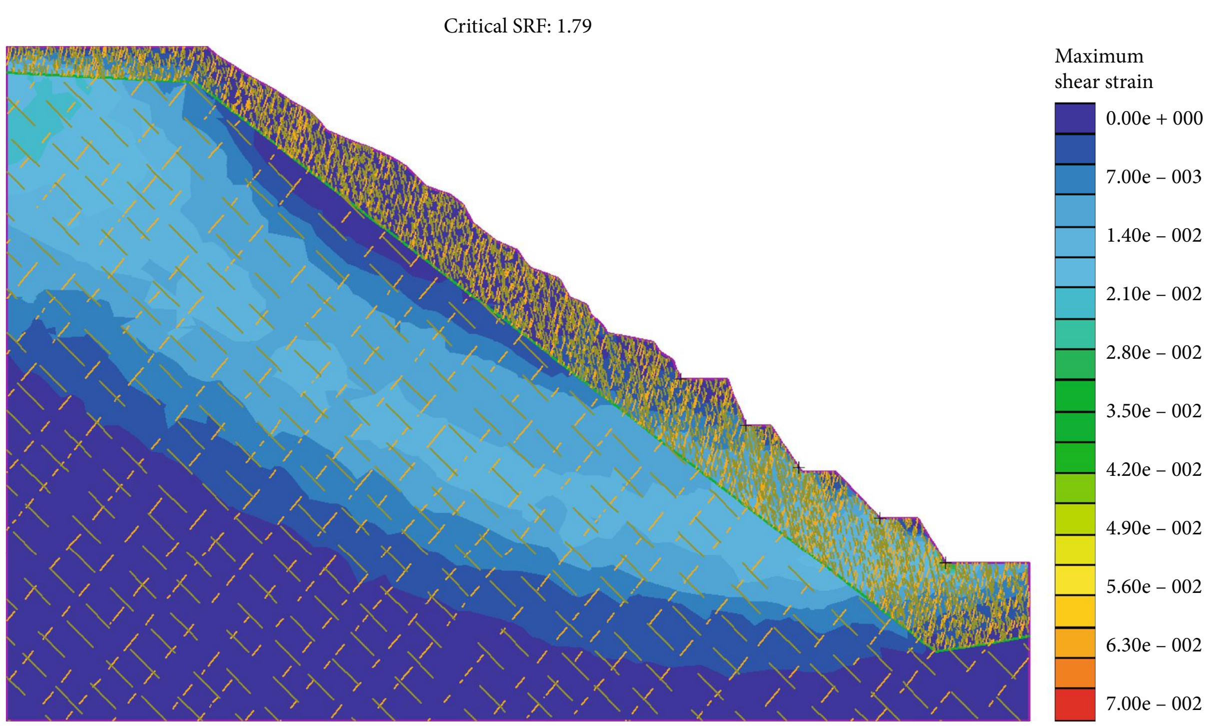

(b) Cloud chart of maximum shear strain for 20 times of the freeze-thaw cycle

Figure 14: Continued.

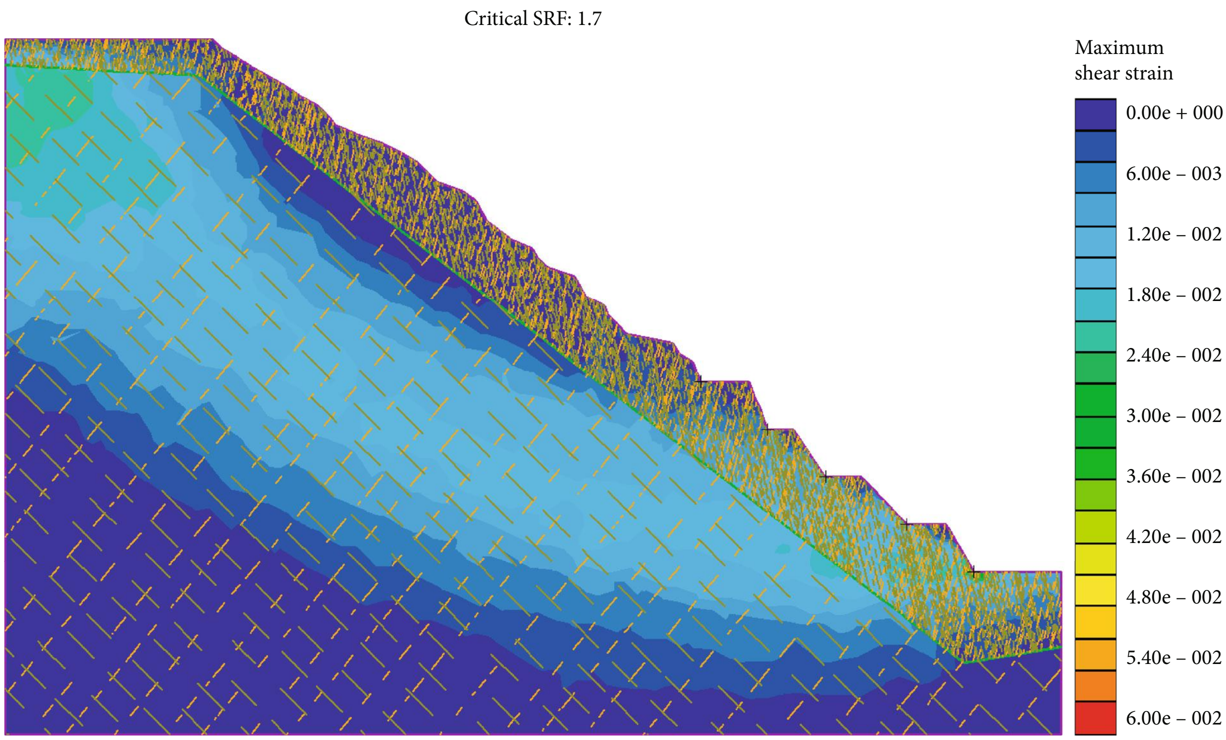

(c) Cloud chart of maximum shear strain for 40 times of the freeze-thaw cycle

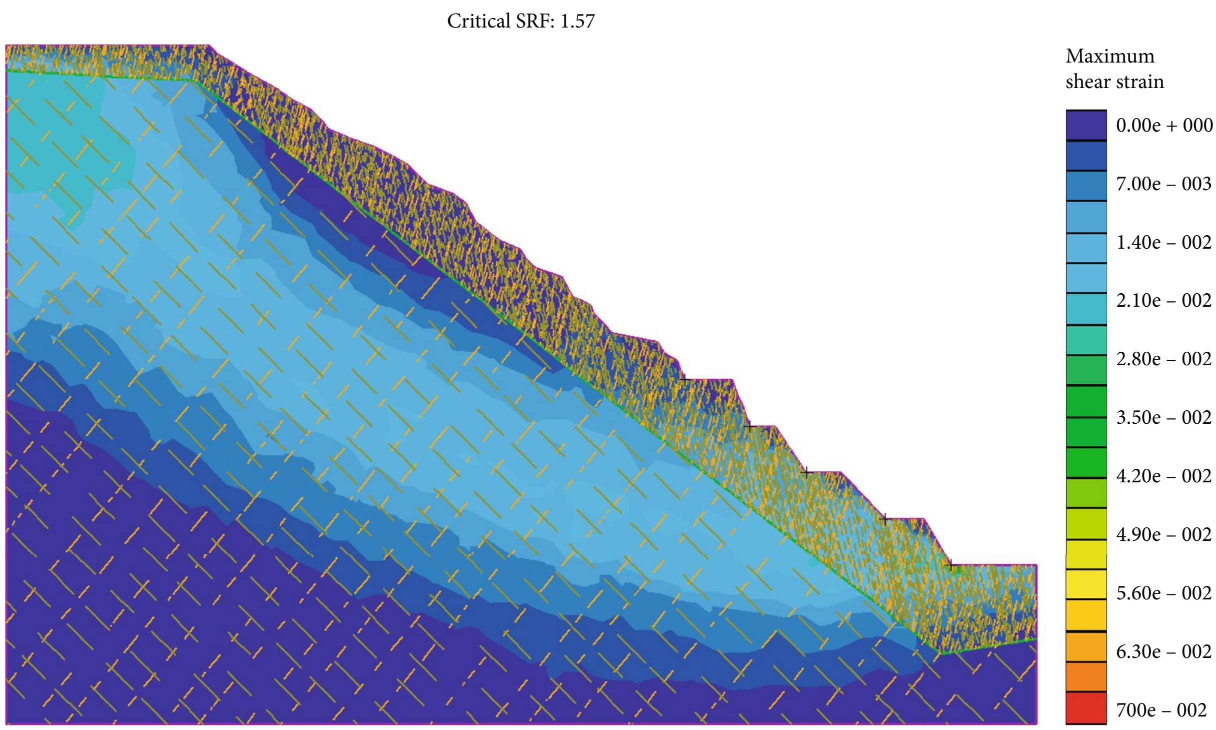

(d) Cloud chart of maximum shear strain for 60 times of the freeze-thaw cycle

Figure 14: Continued.

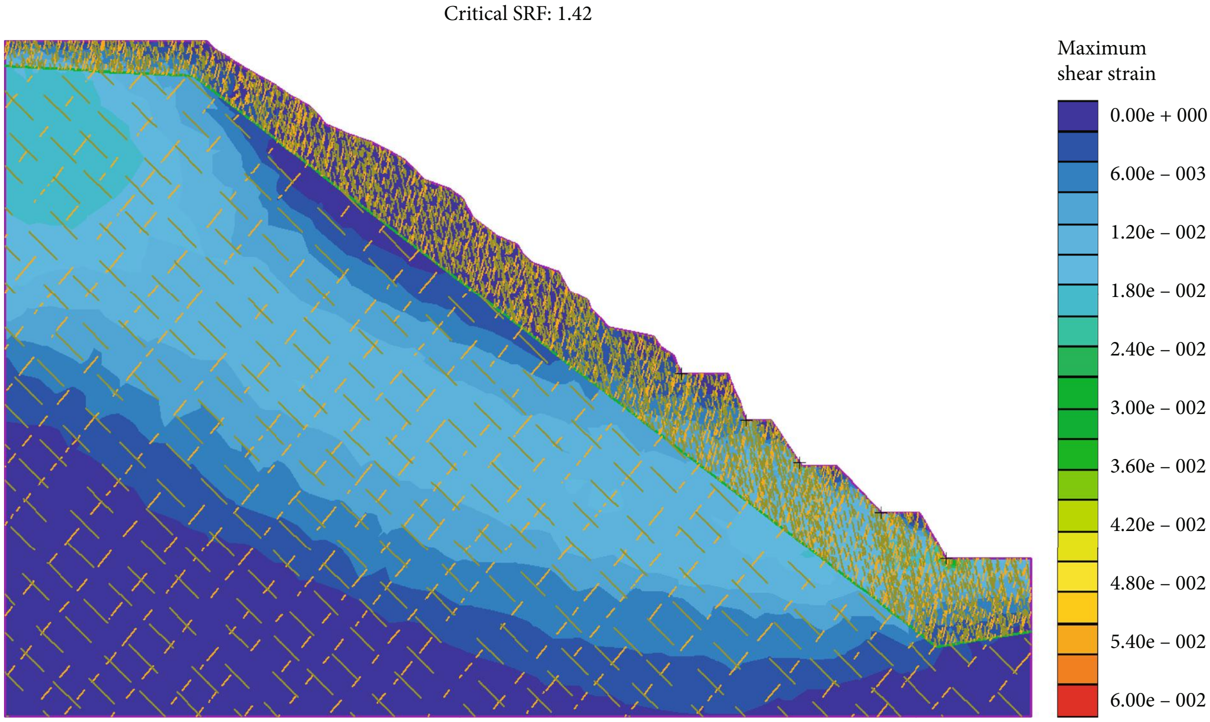

(e) Cloud chart of maximum shear strain for 80 times of the freeze-thaw cycle

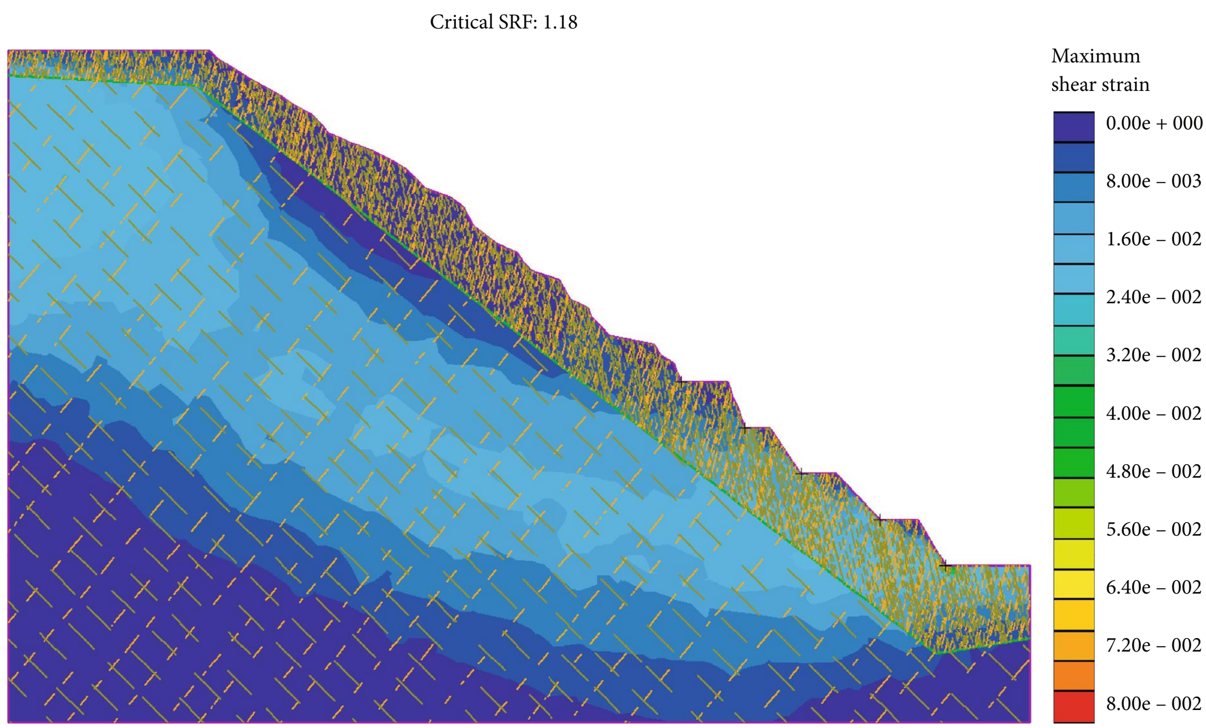

(f) Cloud chart of maximum shear strain for 100 times of the freeze-thaw cycle

Figure 14: Cloud chart of maximum shear strain for different times of the freeze-thaw cycle.

to freeze-thaw damage, and the strength of rock mass decreases. From the numerical simulation results, it can be found that with the increase of the times of the freeze-thaw cycle, the yield elements of the slope are increasing, and their distribution is spreading from the weathered steps above to the steps below. The distribution of yield joints is becoming more and more dense, and they are mainly distributed on the slope surface like the yield elements. In

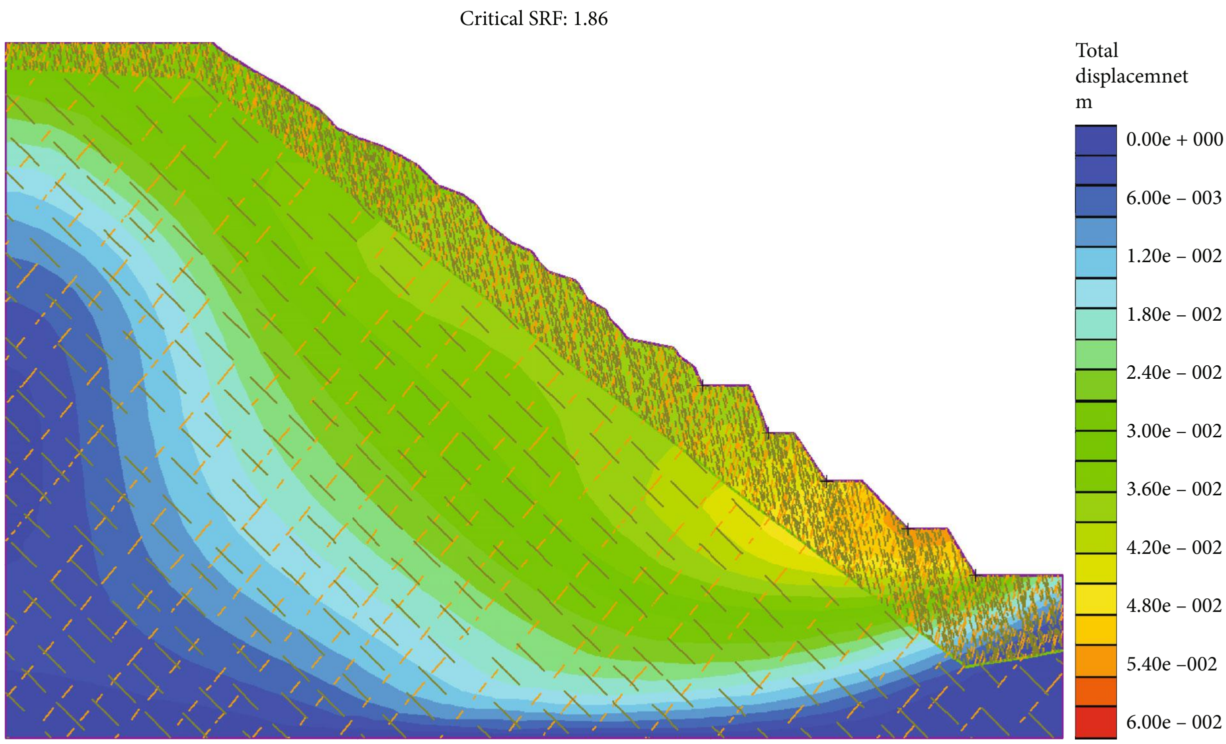

(a) Cloud chart of total displacement for 0 times of the freeze-thaw cycle

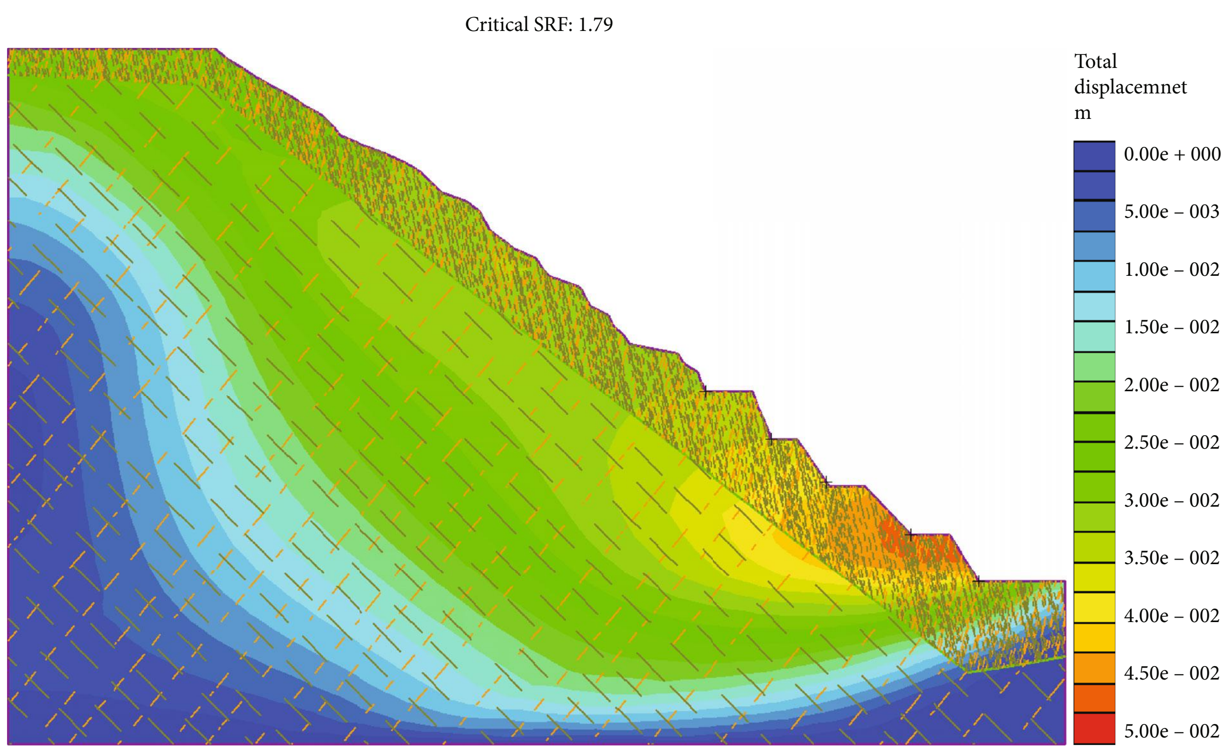

(b) Cloud chart of total displacement for 20 times of the freeze-thaw cycle

Figure 15: Continued.

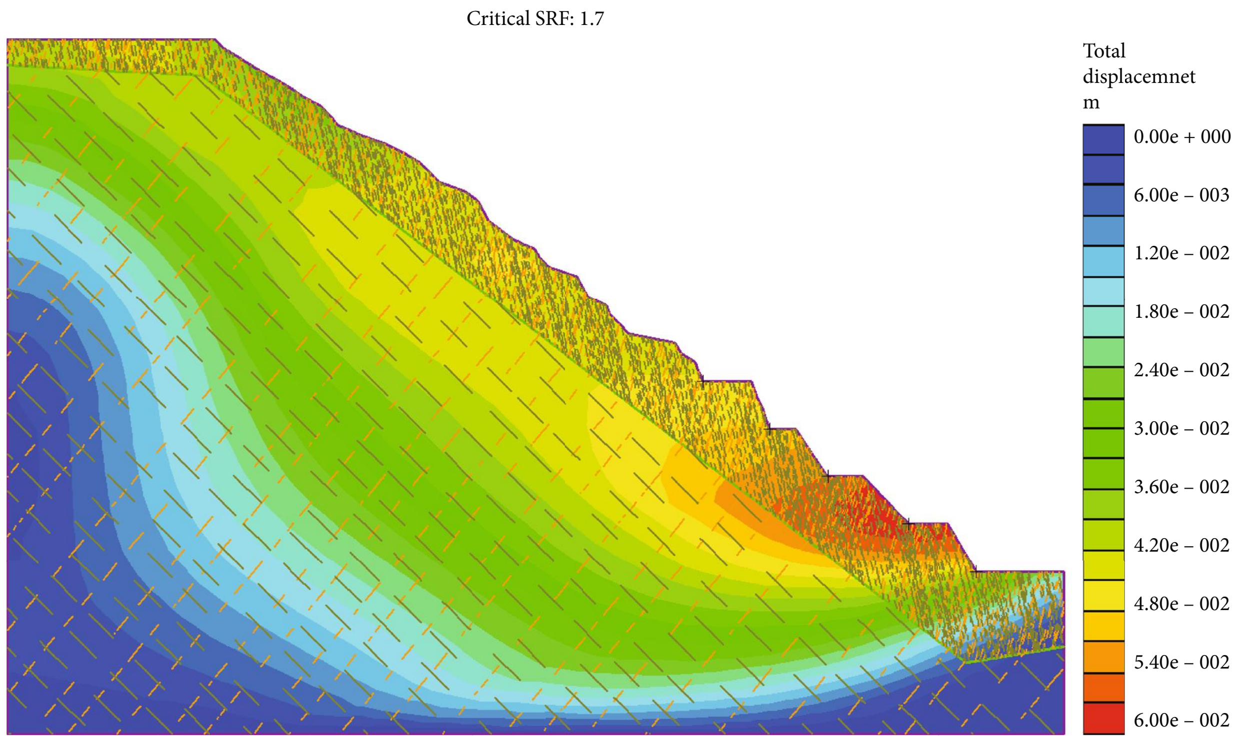

(c) Cloud chart of total displacement for 40 times of the freeze-thaw cycle

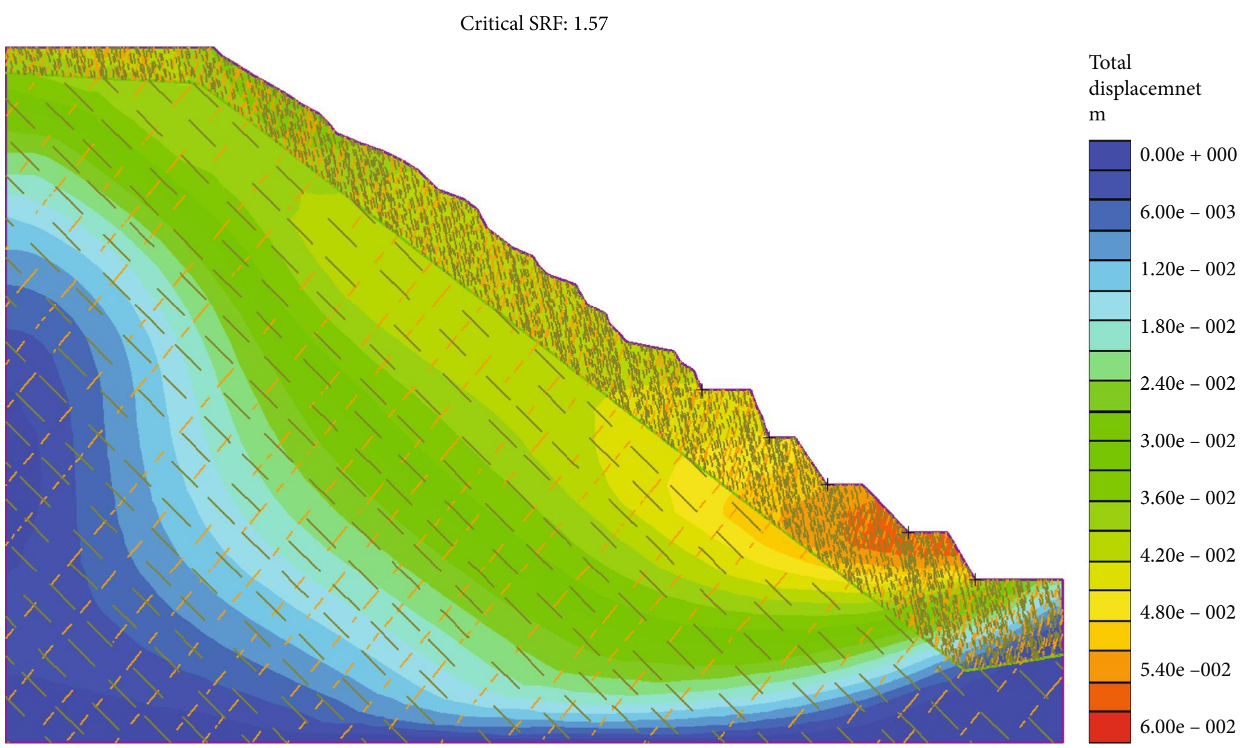

(d) Cloud chart of total displacement for 60 times of the freeze-thaw cycle

Figure 15: Continued.

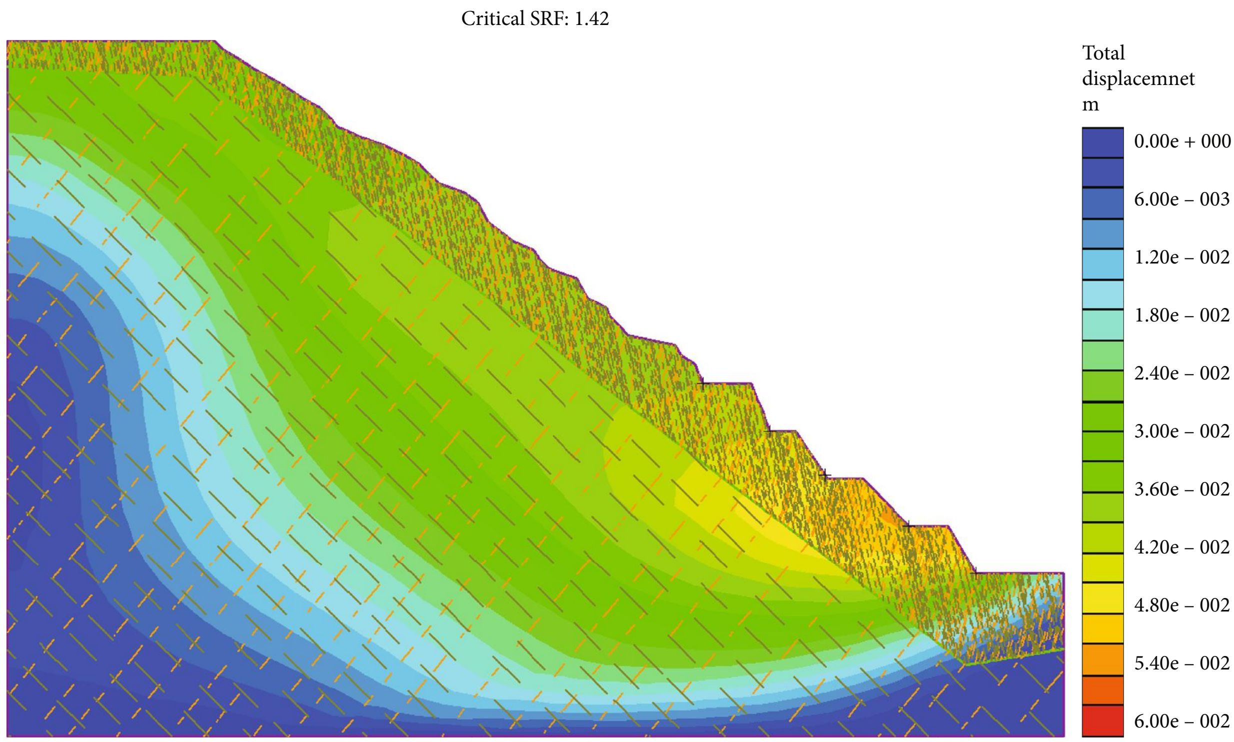

(e) Cloud chart of total displacement for 80 times of the freeze-thaw cycle

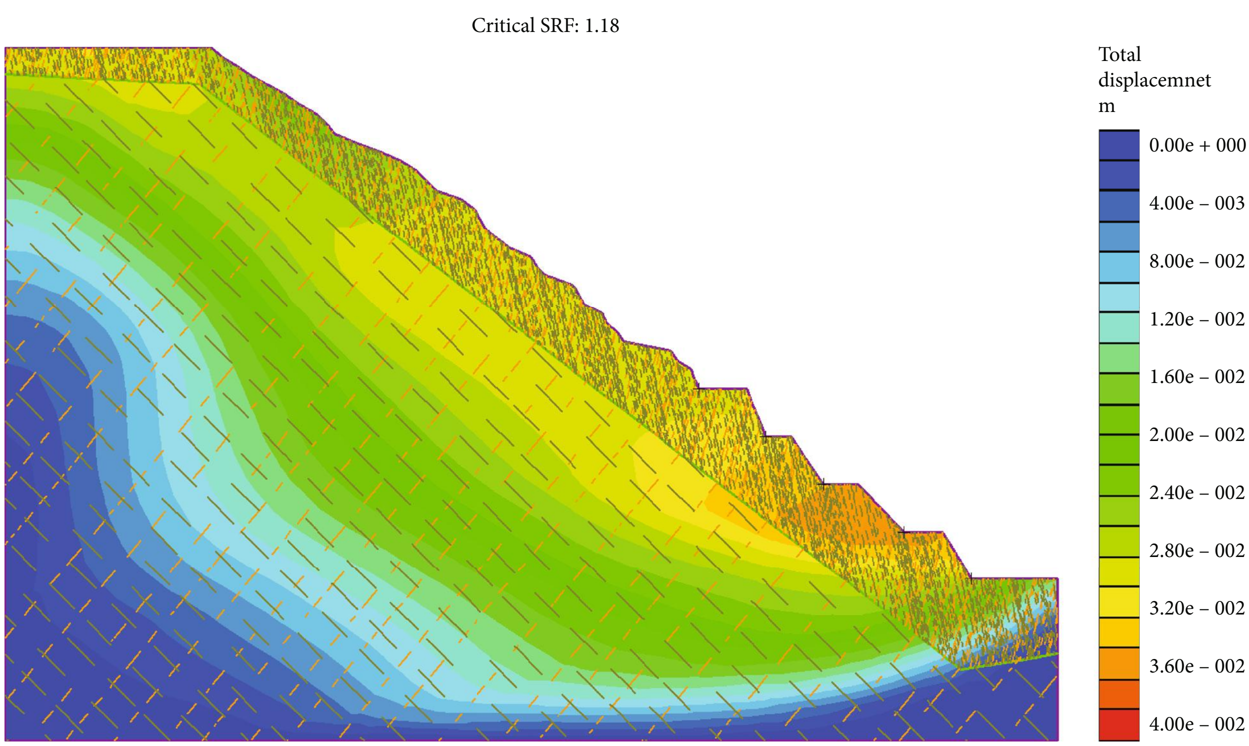

(f) Cloud chart of total displacement for 100 times of the freeze-thaw cycle

FIGURE 15: Cloud chart of total displacement for different times of the freeze-thaw cycle.

order to clearly reflect the changes of the number of yield elements and yield joints, the curves of the number of yield elements and yield joints of the slope with the times of the freeze-thaw cycle are drawn, as shown in Figure 17. They all increase gradually with the increase of the times of the freeze-thaw cycle, and the increasing rate increases first and then decreases.

3.2.4. Analysis of Horizontal Displacement and Strength Reduction Times of Nodes. Figure 12 shows the positions of

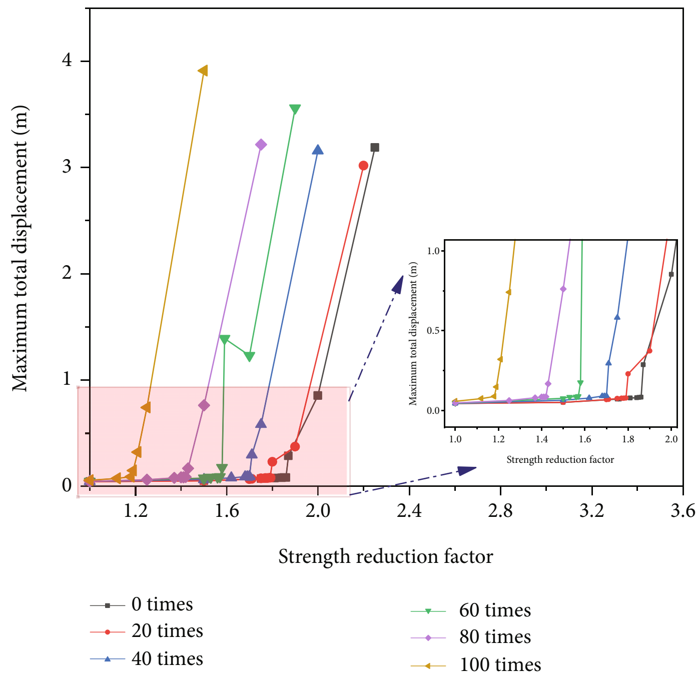

Figure 16: Relationship between strength reduction factor and maximum total displacement of slope under different times of the freeze-thaw cycle.

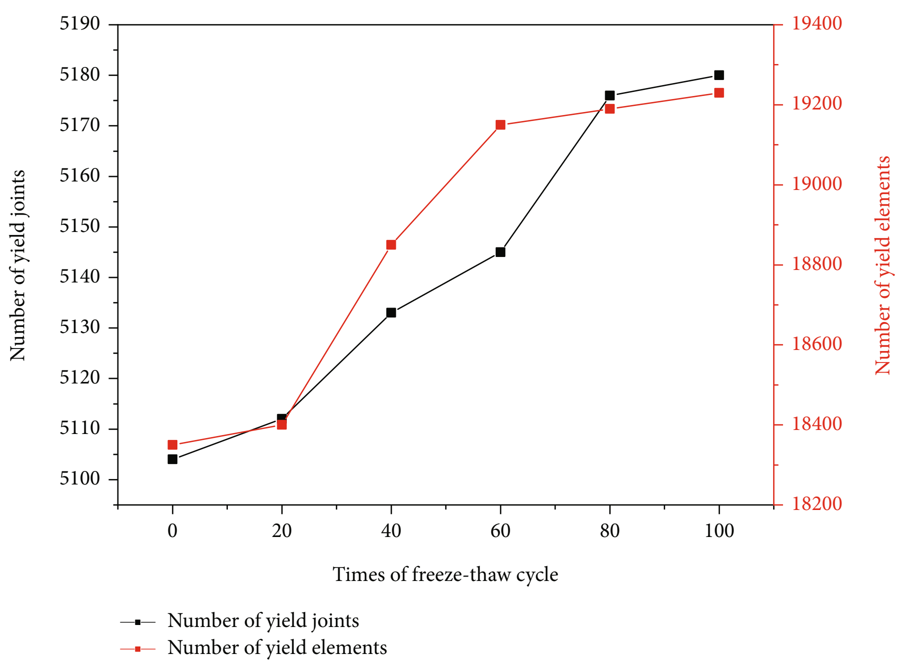

Figure 17: Number of yield elements and yield joints of slope surface.

the five selected nodes in the slope model. By analyzing the relationship between the horizontal displacement and the reduction times of each node under different times of the freeze-thaw cycle, we can further understand the instability and failure of the slope. It can be seen from Figure 18 that the horizontal displacement of the node changes slightly at the beginning, and then, the displacement changes abruptly, indicating that the slope has undergone obvious instability and failure. From node 5 to node 1, the height of the node decreases, and the horizontal displacement of the node also decreases gradually. In addition, the total displacement change of each node and the number of stages corresponding to the mutation decrease gradually with the increase of the times of the freeze-thaw cycle. This result shows that the failure occurs gradually in advance and the slope stability becomes worse.

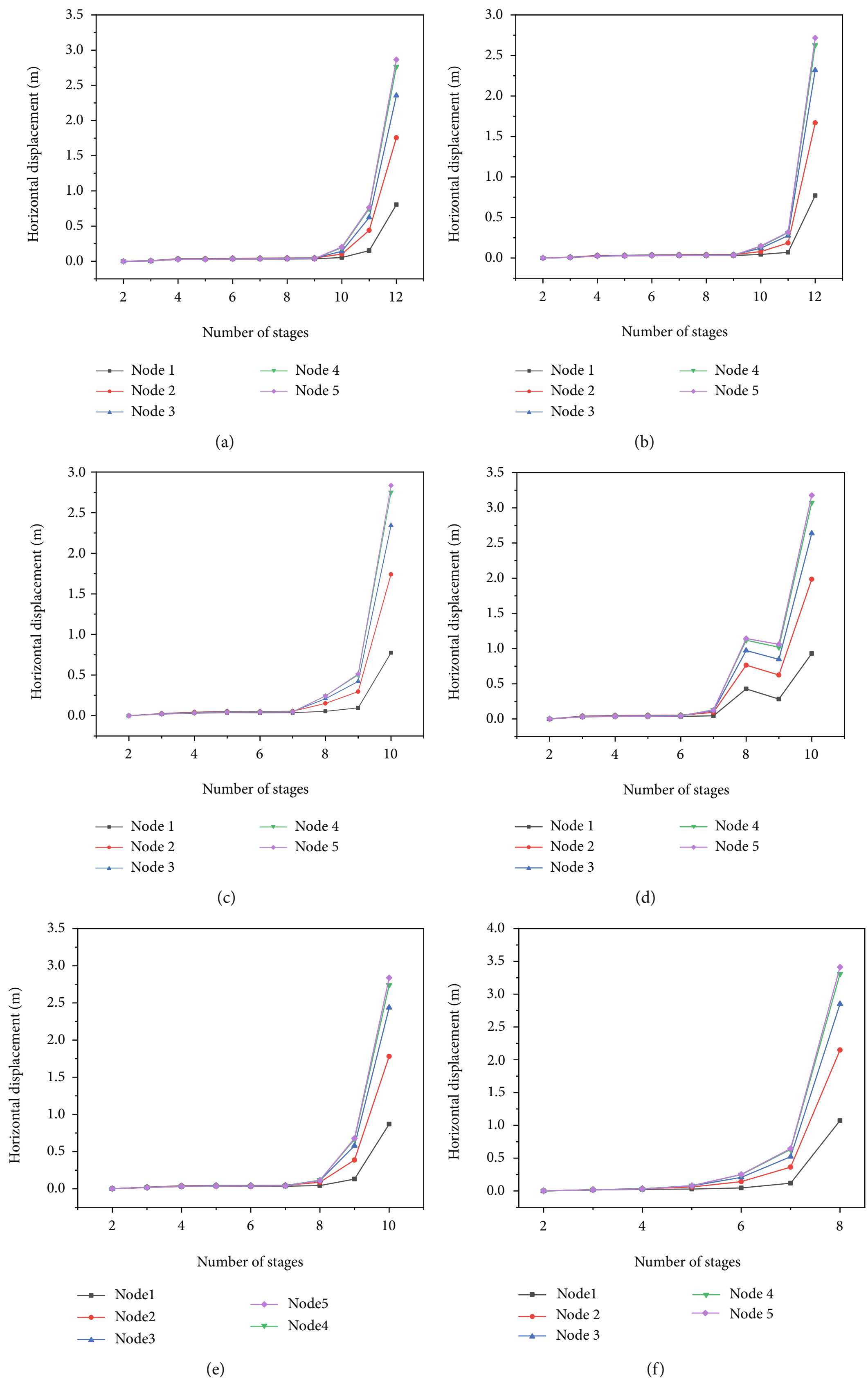

Figure 18: Horizontal displacement curve of each point under different times of the freeze-thaw cycle ((a–f) The times of the freeze-thaw cycle are 0, 20, 40, 60, 80, and 100, respectively).

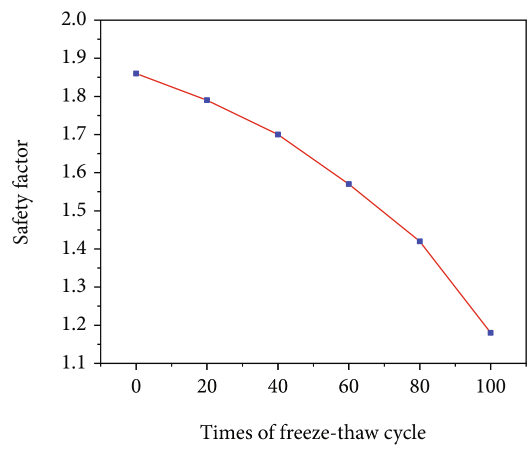

Figure 19: Relationship between safety factor and times of the freeze-thaw cycle.

3.2.5. Analysis of Safety Factor of Slope Model. According to the above analysis, when the times of the freeze-thaw cycle are 0, 20, 40, 60, 80, and 100, the safety factors of the slope are 1.86, 1.79, 1.7, 1.57, 1.42, and 1.18, respectively, and the safety factors are getting smaller and smaller. At the same time, it is found that the reduction ranges of the safety factor are 3.76%, 5.03%, 7.65%, 9.55%, and 16.9%, respectively. The gradually increasing reduction range further shows that the more freeze-thaw cycle, the worse the slope stability. This law can also be found from the trend of the curve in Figure 19. This is because the pore water in the rock mass freezes to form frost heaving force, and the volume expansion leads to the further development of joint fissures. With the increase of the freeze-thaw cycle, the strength of rock slope decreases gradually. Freeze-thaw fatigue damage reduces the physical and mechanical properties of rock, and rock and joints are more prone to yield instability. Therefore, we can understand the freeze-thaw mechanism of rock slope as the cumulative process of rock freeze-thaw damage.

4. Conclusions

In this paper, the influence of the freeze-thaw cycle on the slope stability of an open pit mine is studied with the help of 3D laser scanning technology and RS2 finite element software. The following three conclusions are obtained:

(1) For the point cloud data obtained by 3D laser scanning, firstly, the 3D difference method is used for grid processing. After selecting the discrimination index, all nodes are scanned for flatness detection. After the data is simplified, the improved image segmentation algorithm is used to complete the regional division of the structural plane, and the reasonable flatness detection threshold, regional growth threshold, and area threshold are selected to complete the intelligent recognition of rock mass structural plane

(2) The geometric parameters and other information of rock mass discontinuity are extracted, the plane equation of rock mass discontinuity is fitted by the least square method, and the dip angle of rock mass discontinuity is calculated. The structural plane is divided by K-means cluster analysis method based on occurrence information, and the spacing and equivalent trace length of structural plane are calculated. The calculation results are basically consistent with the actual investigation of the mining area

(3) According to the mechanical parameters obtained from the freeze-thaw cyclic test and the distribution of joint surfaces measured by 3D laser scanning technology, the slope mechanical model is established. The finite element strength reduction method is used to numerically simulate and analyze the slope structural plane, and the safety factor of the slope under different times of the freeze-thaw cycle is calculated. The results show that with the increase of the freeze-thaw cycle, the principal stress, volume strain, and displacement gradually increase. The number of yield elements and yield joints increases gradually, the safety factor decreases continuously, and the stability of the slope becomes worse, which shows that the rocks in high-altitude mining areas are in a freeze-thaw cycle all year round. The freeze-thaw fatigue damage degrades the physical and mechanical properties of rocks, and the rocks and joints are more prone to yield instability

Data Availability

The experimental data used to support the findings of this study are included within the article.

Conflicts of Interest

The authors declare no conflict of interest.

Authors' Contributions

Juzhou Li performed experiments and data analysis. Changhong Li and Guoqing Li did the methodology and conceptualization. Yongyue Hu and Xuefeng Yi did the visualization and data curation and acquired resources. Yu Wang did the supervision, funding acquisition, and project administration;

Acknowledgments

This study was supported by the National Natural Science Foundation of China (52174069), Beijing Natural Science Foundation (8202033), and National Key Technologies Research & Development Program (2018YFC0808402).

References

[1] F. Gu and H. Xie, "Status and development trend of 3D laser scanning technology in the mining field," in *Proceedings Of The 2013 The International Conference On Remote Sensing, Environment And Transportation Engineering (Rsete 2013)*, vol. 31, pp. 407–410, Nanjing, China, 2013.

[2] Y. G. Qin, Z. Q. Luo, W. Wang, and K. H. Zheng, "Cavity 3D Laser Scanning Point Cloud Data Processing Technology," *Journal of Northeastern University (Natural Science)*, vol. 37, no. 11, pp. 1635–1639, 2016.

[3] Y. Wang, X. Yi, J. Han, and Y. Xia, "Acoustic emission and computed tomography investigation on fatigue failure of fissure-contained hollow-cylinder granite: cavity diameter effect," *Fatigue & Fracture of Engineering Materials & Structures*, vol. 45, no. 8, pp. 2243–2260, 2022.

[4] Z. G. Tao, Q. Geng, C. Zhu et al., "The mechanical mechanisms of large-scale toppling failure for counter-inclined rock slopes," *Journal of Geophysics and Engineering*, vol. 16, no. 3, pp. 541–558, 2019.

[5] Q. Wang, S. Xu, M. He, B. Jiang, H. Wei, and Y. Wang, "Dynamic mechanical characteristics and application of constant resistance energy-absorbing supporting material," *International Journal of Mining Science and Technology*, vol. 32, no. 3, pp. 447–458, 2022.

[6] Y. Wang, J. Z. Li, C. Zhu, and T. Mao, "Fatigue failure identification using deformation and energy rate for hole-fissure contained granite under freeze–thaw and variable-frequency–variable-amplitude cyclic loads," *Fatigue & Fracture of Engineering Materials & Structures*, vol. 45, no. 3, pp. 834–851, 2022.

[7] F. Tonon and J. T. Kottenstette, *Laser and photogrammetric methods for rock face characterization*, American Rock Mechanics Association, 2007.

[8] M. Lato, M. S. Diederichs, D. J. Hutchinson, and R. Harrap, "Optimization of LiDAR scanning and processing for automated structural evaluation of discontinuities in rockmasses," *International Journal of Rock Mechanics and Mining Sciences*, vol. 46, no. 1, pp. 194–199, 2009.

[9] M. Vöge, M. J. Lato, and M. S. Diederichs, "Automated rockmass discontinuity mapping from 3-dimensional surface data," *Engineering Geology*, vol. 164, pp. 155–162, 2013.

[10] R. Fanti, G. Gigli, L. Lombardi, D. Tapete, and P. Canuti, "Terrestrial laser scanning for rockfall stability analysis in the cultural heritage site of Pitigliano (Italy)," *Landslides*, vol. 10, no. 4, pp. 409–420, 2013.

[11] W. Kociuba, W. Kubisz, and P. Zagórski, "Use of terrestrial laser scanning (TLS) for monitoring and modelling of geomorphic processes and phenomena at a small and medium spatial scale in Polar environment (Scott River – Spitsbergen)," *Geomorphology*, vol. 212, pp. 84–96, 2014.

[12] A. M. Ferrero, G. Forlani, R. Roncella, and H. I. Voyat, "Advanced geostructural survey methods applied to rock mass characterization," *Rock Mechanics and Rock Engineering*, vol. 42, no. 4, pp. 631–665, 2009.

[13] G. Umili, A. Ferrero, and H. H. Einstein, "A new method for automatic discontinuity traces sampling on rock mass 3D model," *Computational Geosciences*, vol. 51, pp. 182–192, 2013.

[14] S. Chen, M. L. Walske, and I. J. Davies, "Rapid mapping and analysing rock mass discontinuities with 3D terrestrial laser scanning in the underground excavation," *International Journal of Rock Mechanics and Mining Sciences*, vol. 110, pp. 28–35, 2018.

[15] Y. Z. Wang, W. L. Tu, and H. Li, "Fragmentation calculation method for blast muck piles in open–pit copper mines based on three-dimensional laser point cloud data," *International Journal of Applied Earth Observations and Geoinformation*, vol. 100, article 102338, 2021.

[16] R. A. Kromer, A. Abellán, D. J. Hutchinson et al., "Automated terrestrial laser scanning with near-real-time change detection – monitoring of the Séchilienne landslide," *Earth Surface Dynamics*, vol. 5, no. 2, pp. 293–310, 2017.

[17] J. Ma, H. M. Tang, X. L. Hu, R. Yong, H. Xia, and Y. J. Song, "Application of 3D laser scanning technology to landslide physical model test," *Rock and Soil Mechanics*, vol. 35, no. 5, pp. 1495–1505, 2014.

[18] Y. Wang, J. Han, Y. Xia, and D. Long, "New insights into the fracture evolution and instability warning predication for fissure-contained hollow-cylinder granite with different hole diameter under multi-stage cyclic loads," *Theoretical and Applied Fracture Mechanics*, vol. 119, article 103363, 2022.

[19] L. C. Pereira and M. S. Lana, "Stress–strain analysis of buckling failure in phyllite slopes," *Geotechnical & Geological Engineering*, vol. 31, no. 1, pp. 297–314, 2013.

[20] W. Liu, "Experimental and numerical study of rock stratum movement characteristics in longwall mining," *Shock and Vibration*, vol. 2019, Article ID 5041536, 15 pages, 2019.

[21] C. H. C. Silva and M. S. Lana, "Numerical modeling of buckling failure in a mine slope," *Rem: Revista Escola de Minas*, vol. 67, no. 1, pp. 81–86, 2014.

[22] A. T. Arslan, B. Kahraman, M. K. Özfırat, T. Frühwirt, K. Yıldızdağ, and H. Köse, "A parametric study using numerical modelling to assess the stability of marble quarries," *Procedia Engineering*, vol. 191, pp. 646–655, 2017.

[23] K. Adach-Pawelus, "Application of seismic monitoring and numerical modelling in the assessment of possibility of seismic event occurrence in the vicinity of ore remnant," *IOP Conference Series–Earth and Environmental Science*, vol. 221, article 012095, 2019.

[24] Y. Wang, Z. Y. Song, T. Q. Mao, and C. Zhu, "Macro–meso fracture and instability behaviors of hollow-cylinder granite containing fissures subjected to freeze–thaw–fatigue loads," *Rock Mechanics and Rock Engineering*, vol. 55, no. 7, pp. 4051–4071, 2022.